Mon. Not. R. Astron. Soc. **000**, 1–18 (2003) Printed 2 February 2008 (MN LATEX style file v2.2)

Magnetorotational instability in stratified, weakly ionised accretion discs

Raquel Salmeron[1] & Mark Wardle[2]
[1] *School of Physics, University of Sydney, NSW 2006, Australia*
[2] *Physics Department, Macquarie University, NSW 2109, Australia*

arXiv:astro-ph/0307272v1 14 Jul 2003

2003 March 20

ABSTRACT

We present a linear analysis of the vertical structure and growth of the magnetorotational instability in stratified, weakly ionised accretion discs, such as protostellar and quiescent dwarf novae systems. The method includes the effects of the magnetic coupling, the conductivity regime of the fluid and the strength of the magnetic field, which is initially vertical. The conductivity is treated as a tensor and assumed constant with height.

We obtained solutions for the structure and growth rate of global unstable modes for different conductivity regimes, strengths of the initial magnetic field and coupling between ionised and neutral components of the fluid. The envelopes of short-wavelength perturbations are determined by the action of competing local growth rates at different heights, driven by the vertical stratification of the disc. Ambipolar diffusion perturbations peak consistently higher above the midplane than modes including Hall conductivity. For weak coupling, perturbations including the Hall effect grow faster and act over a more extended cross-section of the disc than those obtained using the ambipolar diffusion approximation.

Finally, we derived an approximate criterion for when Hall diffusion determines the growth of the magnetorotational instability. This is satisfied over a wide range of radii in protostellar discs, reducing the extent of the magnetic 'dead zone'. Even if the magnetic coupling is weak, significant accretion may occur close to the midplane, rather than in the surface regions of weakly-ionised discs.

Key words: accretion, accretion discs – instabilities – magnetohydrodynamics – stars: formation.

1 INTRODUCTION

The collapse of protostellar cores lead to the development of a central mass or protostar, surrounded by a disc of material, which is accreted towards the center. During this process angular momentum is transferred to a small percentage of disc material at large radii, enabling the collapse of most of the disc towards the central star (e.g. Weintraub, Sandell & Duncan 1989; Adams, Emerson & Fuller 1990; Beckwith et al. 1990). The evolution of this 'disc accretion' phase is dependent upon the rate of angular momentum transport in the disc (e.g. Adams & Lin 1993).

A variety of mechanisms have been invoked to explain this transport. As the molecular viscosity of accretion discs is too low to explain observed accretion rates (Pringle 1981), some form of turbulent viscosity must be present. The origin and characteristics of this turbulence remains an important problem in star formation theories. Convective turbulence has been considered as an option (Lin & Papaloizou 1980), but further studies suggest that this mechanism may transport angular momentum towards the central star instead of away from it (Cabot & Pollack 1992; Ryu & Goodman 1992; Stone & Balbus 1996). The gravitational field of a companion star may trigger hydrodynamic waves which can transport angular momentum (Vishniac & Diamond 1989; Rozyczka & Spruit 1993), but as a significant fraction of stars do not belong to binary systems, this mechanism is not general enough to explain accretion processes in all stars.

Balbus and Hawley have pointed out that the nature of this anomalous viscosity can be hydromagnetic (Balbus & Hawley 1991; Hawley & Balbus 1991; Stone et al. 1996). This 'magnetorotational' instability (MRI) had been described initially by Velikov (1959) and Chandrasekhar (1961) through their analysis of magnetised Couette flows. It drives turbulent motions which transport angular momentum radially outwards, as fluid elements exchange angular momentum non-locally by means of the distortion of the magnetic field lines that connect them.

Under ideal MHD conditions, MRI perturbations grow

in discs that are differentially rotating, with the angular velocity increasing outwards. Axisymmetric modes need a magnetic field with a weak, poloidal component. In this context, 'weak' means that the magnetic energy density of the field is less than the thermal energy density. These perturbations have a characteristic length scale $\lambda \sim v_A/\Omega$, where v_A is the Alfvén speed and Ω is the keplerian angular frequency in the disc, and a maximum growth rate $\sim q\Omega/2$, with $q \equiv 1.5$ for keplerian discs (Balbus & Hawley 1992a). This growth rate does not depend on the strength or direction of the magnetic field as long as a poloidal component is present. Non-axisymmetric perturbations are most unstable under the influence of a poloidal field, but also grow at a reduced rate if the field is purely toroidal (Balbus & Hawley 1992b). These perturbations are of interest for the analysis of field amplification mechanisms, as dynamo amplification can not occur through axisymmetric perturbations (Moffatt 1978). With no strong dissipation processes, no other conditions are required. Because of its robustness and the general conditions under which it develops, the magnetorotational instability is a promising source of turbulent viscosity in accretion discs.

Ideal MHD conditions are a good approximation to model astrophysical systems where the ionisation fraction of the gas is high enough to ensure neutral and ionised components of the fluid are well coupled. Active dwarf novae (except possibly in the outer regions) and black hole accretion discs are examples of such systems. However, in dense, cool environments such as those of protostellar discs, it is doubtful that magnetic coupling is significant over the entire radial and vertical dimensions of the discs (Gammie 1996; Wardle 1997). Similar conditions are thought to apply in quiescent and the outer regions of hot-state dwarf novae discs (Gammie & Menou 1998; Menou 2000; Stone et al. 2000). In these cases, low conductivity significantly affects the growth and structure of MRI perturbations. Different approximations have been adopted to account for the departure from ideal MHD in low conductivity astrophysical discs (see section 2.1).

Most models of the MRI in low conductivity discs have used the ambipolar diffusion (Blaes & Balbus 1994; MacLow et al. 1995; Hawley & Stone 1998) or resistive (Jin 1996; Balbus & Hawley 1998; Sano, Inutsuka & Miyama 1998) limits. Recently, it has been recognised the importance of the Hall conductivity terms in addition to resistivity for the analysis of low conductivity discs (Wardle 1999, hereafter W99, Balbus & Terquem 2001 and Sano & Stone 2002a,b; 2003).

The huge variation of fluid variables over the vertical and radial extension of astrophysical discs is a further complication. Vertical stratification is particularly relevant, as these objects are generally thin and changes in the plane of the disc are much more gradual than those in the direction perpendicular to it. Previous models of the MRI have not included density stratification and Hall conductivity simultaneously. It is expected that solutions will be strongly modified when both factors are present. This motivates the present study.

This paper examines the structure and linear growth of the magnetorotational instability in vertically stratified, non self-gravitating accretion discs. We assume the disc is isothermal and geometrically thin, so variations in the fluid variables in the radial direction can be ignored. The initial magnetic field is vertical and the analysis is restricted to perturbations with wavevector perpendicular to the plane of the disc ($k = k_z$). These are the most unstable perturbations with the adopted field geometry, as magnetic pressure strongly supresses displacements with $k_r \neq 0$ (Balbus & Hawley 1991, Sano & Miyama 1999). The conductivity of the gas is treated as a tensor and assumed constant with height in this initial study, although the formulation is also valid for a z-dependent conductivity. This makes the present method a powerful tool for the analysis of more realistic discs (see section 6 - Discussion).

Section 2 presents the governing equations for a weakly ionised, magnetised disc in near-keplerian motion around the central star and details the adopted disc model. Section 3 summarises the linearisation of the equations and presents the final linear system in dimensionless form. It also describes the three parameters that control the dynamics of the fluid. Section 4 discusses the boundary conditions used to integrate the equations from the midplane to the surface of the disc and the integration method. Section 5 presents the test cases used to characterise the conductivity regimes relevant for this work and compares our results with a previous local analysis. It also details key findings on the dependency of the structure and growth rate of the perturbations with the conductivity regime, the strength of the magnetic field and its coupling with the neutral gas. These results are discussed in section 6. By way of example, this section also calculates the structure and growth rate of the MRI under fluid conditions where different conductivity regimes are dominant at different heights above the midplane. This reflects (qualitatively) the conditions expected to be found in real discs. Finally, the methodology and key findings of this paper are summarised in section 7.

2 FORMULATION

2.1 Governing Equations

The equations of non-ideal MHD are written about a local keplerian frame corotating with the disc at the angular frequency Ω associated with the particular radius of interest. Consequently, the velocity of the fluid can be expressed as a departure from exact keplerian motion $\boldsymbol{v} = \boldsymbol{V} - \boldsymbol{v}_K$, where $\boldsymbol{V}$ is the velocity in the standard laboratory coordinate system (r, ϕ, z) anchored at the central mass M, and $\boldsymbol{v}_K = \sqrt{GM/r}\hat{\boldsymbol{\phi}}$ is the keplerian velocity at the radius r. Similarly, if $\partial/\partial t$ is the time derivative in the local keplerian frame, then the time derivative in the laboratory frame can be expressed as $\partial/\partial t + \Omega\partial/\partial\phi$. We also assume that the fluid is weakly ionised, meaning that the abundances of charged species are so low that their inertia and thermal pressure, as well as the effect of ionisation and recombination processes in the neutral gas, are negligible. These assumptions effectively restrict the range of frequencies that can be studied with this formulation to be smaller than the collision frequency of any of the charged species with the neutrals. Accordingly, separate equations of motion for the charged species are not required and their effect on the neutrals is contained in a conductivity tensor (see section 2.2).

The governing equations are the continuity equation,

$$\frac{\partial \rho}{\partial t} + \nabla \cdot (\rho \boldsymbol{v}) = 0\,, \tag{1}$$

the equation of motion,

$$\frac{\partial \boldsymbol{v}}{\partial t} + (\boldsymbol{v}\cdot\nabla)\boldsymbol{v} - 2\Omega v_\phi \hat{\boldsymbol{r}} + \tfrac{1}{2}\Omega v_r \hat{\boldsymbol{\phi}} - \frac{v_K^2}{r}\hat{\boldsymbol{r}} + \frac{c_s^2}{\rho}\nabla\rho + \\ + \nabla\Phi - \frac{\boldsymbol{J}\times\boldsymbol{B}}{c\rho} = 0\,, \tag{2}$$

and the induction equation,

$$\frac{\partial \boldsymbol{B}}{\partial t} = \nabla\times(\boldsymbol{v}\times\boldsymbol{B}) - c\nabla\times\boldsymbol{E}' - \tfrac{3}{2}\Omega B_r\hat{\boldsymbol{\phi}}\,. \tag{3}$$

In the equation of motion (2), Φ is the gravitational potential due to the central gas, given by

$$\Phi = -\frac{GM}{(r^2+z^2)^{\frac{1}{2}}}\,, \tag{4}$$

and $\boldsymbol{v}_K^2/r$ is the centripetal term generated by exact keplerian motion. At the disc midplane this term balances the radial component of the gravitational potential. The terms $2\Omega v_\phi\hat{\boldsymbol{r}}$ and $\frac{1}{2}\Omega v_r\hat{\boldsymbol{\phi}}$ are the coriolis terms associated with the use of a local keplerian frame, $c_s = \sqrt{P/\rho}$ is the isothermal sound speed, $\Omega = \boldsymbol{v}_K/r$ is the keplerian frequency and c is the speed of light. Other symbols have their usual meanings.

In the induction equation (3), the term $c\nabla\times\boldsymbol{E}'$contains the effects of non-ideal MHD. $\boldsymbol{E}'$ is the electric field in the frame comoving with the neutrals and the term $\frac{3}{2}\Omega\boldsymbol{B}_r\hat{\boldsymbol{\phi}}$ accounts for the generation of toroidal field from the radial component due to the differential rotation of the disc.

Additionally, the magnetic field must satisfy the constraint:

$$\nabla\cdot\boldsymbol{B} = 0\,, \tag{5}$$

and the current density must satisfy Ampere's law,

$$\boldsymbol{J} = \frac{c}{4\pi}\nabla\times\boldsymbol{B} \tag{6}$$

and Ohm's law,

$$\boldsymbol{J} = \boldsymbol{\sigma}\cdot\boldsymbol{E}'\,. \tag{7}$$

Note that the conductivity, which depends on the abundance and drifts of the charged species through the neutral gas is treated as a tensor $\boldsymbol{\sigma}$, as detailed in the following section. This formulation is compared to the drift velocity approach in section 2.3.

2.2 The conductivity tensor $\boldsymbol{\sigma}$

The electric conductivity is a tensor whenever the gyrofrequency of the charged carriers is larger than the frequency of momentum exchange by collisions with the neutrals, or $|\beta| \gg 1$ (Cowling 1957, Norman & Hayvaerts 1985, Nakano & Umebayashi 1986). On the contrary, when collisions with the neutrals are dominant the conductivity is a scalar, the ordinary ohmic resistivity. To obtain expressions for the components of this tensor, we begin by writing down the equations of motion of the ionised species. As inertia and thermal pressure are neglected, the motion of the charged particles is given by the balance of the Lorentz force and the drag force from collisions with the neutrals,

$$Z_j e\left(\boldsymbol{E}' + \frac{\boldsymbol{v}_j}{c}\times\boldsymbol{B}\right) - \gamma_j m_j \boldsymbol{v}_j = 0\,, \tag{8}$$

where each charged species j is characterised by its number density n_j, particle mass m_j, charge $Z_j e$ and drift velocity $\boldsymbol{v}_j$. In the above equation,

$$\gamma_j = \frac{<\sigma v>_j}{m_j + m}\,, \tag{9}$$

where m is the mean mass of the neutral particles and $<\sigma v>_j$ is the rate coefficient of momentum exchange by collisions with the neutrals. We will also make use of the Hall parameter,

$$\beta_j = \frac{Z_j e B}{m_j c}\,\frac{1}{\gamma_j \rho}\,, \tag{10}$$

given by the ratio of the gyrofrequency and the collision frequency of charged species j with the neutrals. It represents the relative importance of the Lorentz and drag terms in equation (8).

Following the treatment of Wardle & Ng (1999) and W99 we use the following expression for Ohm's law,

$$\boldsymbol{J} = \boldsymbol{\sigma}\cdot\boldsymbol{E}' = \sigma_\parallel \boldsymbol{E}'_\parallel + \sigma_1 \hat{\boldsymbol{B}}\times\boldsymbol{E}'_\perp + \sigma_2 \boldsymbol{E}'_\perp\,, \tag{11}$$

obtained by inverting (8) to express $\boldsymbol{v}_j$ as a function of $\boldsymbol{E}'$ and $\boldsymbol{B}$ and then using $\boldsymbol{J} = e\sum_j n_j Z_j \boldsymbol{v}_j$ together with the charge neutrality assumption $\sum_j n_j Z_j = 0$. In equation (11), $\boldsymbol{E}'_\parallel$ and $\boldsymbol{E}'_\perp$ are the components of the electric field $\boldsymbol{E}'$, parallel and perpendicular to the magnetic field, respectively. The components of the conductivity tensor $\boldsymbol{\sigma}$ are the conductivity parallel to the magnetic field,

$$\sigma_\parallel = \frac{ec}{B}\sum_j n_j Z_j \beta_j\,, \tag{12}$$

the Hall conductivity,

$$\sigma_1 = \frac{ec}{B}\sum_j \frac{n_j Z_j}{1+\beta_j^2}\,, \tag{13}$$

and the Pedersen conductivity,

$$\sigma_2 = \frac{ec}{B}\sum_j \frac{n_j Z_j \beta_j}{1+\beta_j^2}\,. \tag{14}$$

The relative values of the components of the conductivity tensor differentiate three conductivity regimes:

(i) The *ambipolar diffusion* regime occurs when $\sigma_\parallel \gg \sigma_2 \gg |\sigma_1|$, or $|\beta| \gg 1$ for most charged species. This implies that most charged particles are strongly tied to the magnetic field by electromagnetic stresses. This regime is dominant at relatively low densities, where the magnetic field is frozen into the ionised component of the fluid and drifts with it through the neutrals. The linear behaviour of the MRI in this regime has been analysed by Blaes & Balbus (1994) and the non-linear growth by MacLow et al. (1995) and Hawley & Stone (1998).

(ii) The *resistive (Ohmic)* regime is obtained when most charged species are linked to the neutrals via collisions. This occurs when $\sigma_\parallel \approx \sigma_2 \gg |\sigma_1|$, implying $|\beta| \ll 1$. This regime is predominant closest to the midplane, where the high density makes the collision frequency of the charged particles with the neutrals high enough to prevent the former from drifting. This case has been studied under a linear approximation by Jin (1996), Balbus & Hawley (1998), Papaloizou

& Terquem (1997), Sano & Miyama (1999) and Sano et. al. (2000). The non-linear regime has been studied by Sano et al. (1998); Fleming, Stone & Hawley (2000) and Stone & Fleming, (2003). This last work includes a z-dependent resistivity.

(iii) Finally, the *Hall* regime occurs when charged particles of one sign are tied to the magnetic field while those of the other sign follow the neutrals. In this case $|\sigma_1| \sim \sigma_2 < \sigma_\parallel$ and $|\beta| \approx 1$. It is important at intermediate densities, between the ones associated with the ambipolar and Ohmic difussion regimes. Recent studies have explored the MRI with Hall effects in the linear (W99, Balbus & Terquem 2001) and non-linear regimes (Sano & Stone 2002a,b; 2003).

2.3 Comparison with the multifluid approach

Another commonly used form of the induction equation is obtained by assuming that ions and electrons are the main charge carriers and drift through the neutrals (e.g Balbus & Terquem 2001, Sano & Stone 2002). Using this approach, the induction equation is

$$\begin{aligned}\frac{\partial \boldsymbol{B}}{\partial t} &= \nabla \times (\boldsymbol{v}_e \times \boldsymbol{B}) \\ &= \nabla \times \left[\boldsymbol{v} \times \boldsymbol{B} - \frac{4\pi\eta \boldsymbol{J}}{c} - \frac{\boldsymbol{J} \times \boldsymbol{B}}{e n_e} + \frac{(\boldsymbol{J} \times \boldsymbol{B}) \times \boldsymbol{B}}{c \gamma_i \rho \rho_i} \right]\end{aligned} \tag{15}$$

where $\boldsymbol{v}_e$ is the electron drift speed, $\eta = c^2/4\pi\sigma$ is the resistivity and subscripts e and i refer to electrons and ions, respectively. The four terms in the right hand side of equation (15) are, from left to right, the inductive, resistive, Hall and ambipolar diffusion terms. We now express equation (3) in terms of $\boldsymbol{J}$, $\boldsymbol{B}$ and the components of the conductivity tensor in order to show that, in the appropriate limit, it corresponds to equation (15), as expected. We begin by inverting equation (11) to find an expression for $\boldsymbol{E}'$,

$$\boldsymbol{E}' = \frac{\boldsymbol{J}}{\sigma_\parallel} + \frac{\sigma_1}{\sigma_\perp^2} \frac{\boldsymbol{J} \times \boldsymbol{B}}{B} - \left(\frac{\sigma_2}{\sigma_\perp^2} - \frac{1}{\sigma_\parallel} \right) \frac{(\boldsymbol{J} \times \boldsymbol{B}) \times \boldsymbol{B}}{B^2} \tag{16}$$

where $\sigma_\perp = \sqrt{\sigma_1^2 + \sigma_2^2}$ is the total conductivity perpendicular to the magnetic field. Assuming that the only charged species are ions and electrons with Hall parameters β_i and β_e (< 0), respectively, and that charge neutrality is satisfied ($n_i = n_e$), we obtain the following expressions for the components of the conductivity tensor:

$$\sigma_\parallel = \frac{c e n_e}{B} (\beta_i - \beta_e) \,, \tag{17}$$

$$\sigma_1 = \frac{c e n_e}{B} \frac{(\beta_i + \beta_e)(\beta_e - \beta_i)}{(1 + \beta_e^2)(1 + \beta_i^2)} \,, \text{ and} \tag{18}$$

$$\sigma_2 = \frac{c e n_e}{B} \frac{(1 - \beta_i \beta_e)(\beta_i - \beta_e)}{(1 + \beta_e^2)(1 + \beta_i^2)} \,. \tag{19}$$

From (18) and (19), we find:

$$\sigma_\perp = \frac{c e n_e}{B} \frac{(\beta_i - \beta_e)}{[(1 + \beta_e^2)(1 + \beta_i^2)]^{1/2}} \,. \tag{20}$$

Substituting these expressions into (16) gives

$$\boldsymbol{E}' = \frac{\beta_e}{\beta_i - \beta_e} \frac{\boldsymbol{J}}{\sigma} + \frac{\beta_e + \beta_i}{\beta_e - \beta_i} \frac{\boldsymbol{J} \times \boldsymbol{B}}{c e n_e} - \frac{\beta_e}{\beta_e - \beta_i} \frac{(\boldsymbol{J} \times \boldsymbol{B}) \times \boldsymbol{B}}{c^2 \gamma_i \rho \rho_i} \tag{21}$$

where σ is the electrical conductivity due to electrons. Finally, simplifying (21) by using $|\beta_e| \gg \beta_i$ (as is the case) and substituting the resulting $\boldsymbol{E}'$ in equation (3) (without the coriolis term), yields the standard result, shown in (15).

Each of the last three terms in the right hand side of equation (15) dominate when the fluid is in a particular conductivity regime (section 2.2). These limits can also be recovered with the appropriate assumptions, through equations (16) and (21). To get the resistive regime, for example, we substitute $\sigma_1 = 0$ and $\sigma_\parallel = \sigma_2$ into equation (16). In this limit the conductivity is a scalar (the resistive approximation), so $\boldsymbol{E}' = \boldsymbol{J}/\sigma$ and the induction equation reduces to the familiar form,

$$\frac{\partial \boldsymbol{B}}{\partial t} = \nabla \times \left[\boldsymbol{v} \times \boldsymbol{B} - \frac{c^2}{4\pi\sigma} \nabla \times \boldsymbol{B} \right] \,. \tag{22}$$

On the other hand, to model the Hall limit, we regard the charged species to be either 'ions', which are strongly tied to the neutrals through collisions ($\beta_i \ll 1$), or 'electrons', for which the only important forces are electromagnetic stresses ($|\beta_e| \gg 1$) (see also discussion in W99). In this limit the Hall conductivity is

$$|\sigma_1| = \frac{c e n_e}{B} \tag{23}$$

while the Pedersen conductivity is

$$\sigma_2 = |\sigma_1| \left(\beta_i - \frac{1}{\beta_e} \right) \ll \sigma_1 \,. \tag{24}$$

As the ions are effectively locked with the neutrals, the current density will be given by the drift of the electrons through the neutral gas. Collisions are unimportant in their equation of motion, so they drift perpendicular to the plane of the electric and magnetic fields, in order to annul the Lorentz force acting upon them. In this limit $(\boldsymbol{J} \times \boldsymbol{B}) \times \boldsymbol{B} = -\boldsymbol{J}$ and

$$\boldsymbol{E}' = \frac{\boldsymbol{J} \times \boldsymbol{B}}{c e n_e} \,, \tag{25}$$

consistent with the Hall term in equation (15).

Finally, the ambipolar diffusion approximation is recovered by assuming $\sigma_\parallel \gg \sigma_2$, $\sigma_1 = 0$ and $|\beta_e| \gg \beta_i \gg 1$. In this limit, the Pedersen conductivity is given by

$$\sigma_2 = \frac{c e}{B} \frac{n_i}{\beta_i} \,, \text{ and} \tag{26}$$

$$\boldsymbol{E}' = -\frac{(\boldsymbol{J} \times \boldsymbol{B}) \times \boldsymbol{B}}{c^2 \gamma_i \rho \rho_i} \,, \tag{27}$$

which originates the ambipolar diffusion term of (15).

Although the multifluid drift and conductivity tensor formulations are ultimately equivalent, which one is more convenient depends on the problem at hand. In particular, the presence of dust grains tends to make the treatment of different species especially complex. In protostellar discs, dust grains can be the more abundant charged species over extended regions. For example, assuming $0.1\,\mu$m grains, negatively charged grains dominate whenever $n_H \gtrsim 10^{11}$ cm^{-3}, while positive charged grains are the most abundant ions for $n_H \gtrsim 10^{14}$ cm^{-3} (Wardle & Ng 1999). Having separate equations of motion for different charged species would generally involve dividing the grain size distribution of interest

into an appropriate number of discrete intervals and explicitly treating each one. Unless the number of such intervals is small it is easy to see that this method can become very cumbersome. In these circumstances, incorporating the contribution of each charged species into a conductivity tensor can be a valuable approach.

2.4 Disc Model

Our model incorporates the vertical structure of the disc, but neglects fluid variations in the radial direction. This is appropriate as astrophysical accretion discs are generally thin and changes in the radial direction occur in a much bigger length scale than those in the vertical direction. Including the vertical structure means that perturbations of spatial dimensions comparable to the scale height of the disc, which are associated with a strong magnetic field ($v_A \sim c_s$), or low conductivity, can be explored.

The balance between the vertical component of the central gravitational force and the pressure gradient within the disc determines its equilibrium structure. The vertical density distribution in hydrostatic equilibrium is given by

$$\frac{\rho(r,z)}{\rho_o(r)} = \exp\left(-\frac{z^2}{2H^2(r)}\right) . \tag{28}$$

In the above equation, $\rho_o(r)$ is the gas density at the midplane and $H(r) = c_s/\Omega$ is the scaleheight of the disc.

A self-consistent treatment of this problem, would involve adopting a particular dependency of ρ_o and H with r using a suitable model, such as the minimum solar nebula (Hayashi, Nakazawa & Nakagawa 1985) and calculating $\rho(r,z)$ by means of (28). This density, together with the adopted strength of the magnetic field $\boldsymbol{B}$ and the values of the conductivity tensor $\boldsymbol{\sigma}$ as a function of height would be used to evaluate the parameters that govern the fluid evolution (see section 3.3) and solve the fluid equations.

The realistic evaluation of the conductivity tensor is a complex undertaking, as it depends critically on the abundances of charged species (ions, electrons and charged dust grains) which, in turn, are a function of the ionisation balance in the disc. This balance is given by the equilibrium between ionisation processes by cosmic rays, radioactive elements and X-rays from the central star (e.g. Hayashi 1981; Glassgold, Najita & Igea 1997, Igea & Glassgold 1999; Fromang, Terquem & Balbus 2002) and recombinations taking place both in the gas phase and in grain surfaces (e.g. Nishi, Nakano & Umebayashi 1991). In low conductivity discs, the level of ionisation is insufficient to produce good coupling between the magnetic field and the neutral component of the fluid over their entire vertical structure. In protostellar discs, for example, it is expected that in the region outside ~ 0.1 AU from the central star, the coupling will be significant only in the surface layers, where X-rays and cosmic rays can penetrate and ionise the gas (Gammie 1996; Wardle 1997). In these environments, the z-dependent atenuation of the ionisation rate typical of interstellar space $10^{-17}\mathrm{H}^{-1}\ \mathrm{s}^{-1}$ has to be taken into account.

On the other hand, the contribution of dust grains to recombination processes is particularly complex, because they generally have a distribution of sizes and corresponding collision cross sections (Mathis, Rumpl & Nordsieck 1977; Umebayashi & Nakano 1990). Moreover, the dynamics of grain particles depends on the activity of the disc. In quiescent environments, they tend to settle towards the midplane and begin to agglomerate into bigger structures that could eventually become planets (e.g. Weidenschilling & Cuzzi 1993). This removes grains from regions at relatively high z and causes the ionisation level to increase by reducing recombination processes taking place in their surfaces. Simulations of the evolution of dust grain distributions in dense cores show that they grow icy mantles and coagulate efficiently (Ossenkopf 1993). By this process, the smallest particles grow quickly while the upper grain size limit is only slightly changed (Ossenkopf 1993). As a result, the surface area of dust grains can be significantly modified by grain evolution, which ultimately affects the ionisation balance in the disc.

In the present work, a simpler treatment has been adopted. In order to study the MRI under different conductivity regimes, the values of the components of the conductivity tensor have been selected so that they satisfy the conditions outlined in section 2.2 for each regime. For simplicity, these values are assumed to be constant, although the formulation allows them to be a function of height. We found that the parameters that control the evolution of the fluid are the ratio of the components of the conductivity tensor perpendicular to the magnetic field (σ_1/σ_2), the strength of the magnetic field and its degree of coupling with the neutral component of the fluid (see section 3.3). The midplane values of these parameters have been selected in order to simulate the fluid conditions we were interested in modelling. This approach will be discussed in section 5.1 where the chosen test cases are detailed.

With this approach we are able to study the dependency of the growth rate and structure (characterised by the height of maximum amplitude and the wavenumber of unstable modes) of the instability with the parameters of the fluid in a stratified disc. This is relevant, as the region where linear perturbations peak is also expected to be the region where non-linear perturbations grow fastest, until turbulence finally sets in and causes all wavenumbers to interact so that, eventually, the longest wavelengths carry the greatest angular momentum transport (e.g. Hawley & Balbus 1995).

3 LINEARISATION

We linearised the system of equations (1) - (3), (6) and (11) about an initial steady state where $\boldsymbol{J} = \boldsymbol{v} = \boldsymbol{E}' = 0$ and $\boldsymbol{B} = B\hat{z}$. In the initial state both $\boldsymbol{E}'$ and $\boldsymbol{J}$ vanish, so the changes in the conductivity tensor due to the perturbations do not appear in the linearised equations. As a result, it is not necessary to explore how the perturbations affect the conductivity and only the values in the initial steady state are required.

3.1 Linearised Equations

We assume the wavevector of the perturbations is perpendicular to the plane of the disc ($k = k_z$). Perturbations with a vertical wavenumber, initiated from a vertically aligned equilibrium magnetic field, exhibit the fastest growth rate for a given set of parameters because magnetic pressure strongly suppresses displacements with $k_r \neq 0$ (Balbus &

Hawley 1991; Sano & Miyama 1999). Taking perturbations of the form $\boldsymbol{q} = \boldsymbol{q}_0 + \boldsymbol{\delta q}(z)e^{i\omega t}$ about the initial state, linearising and neglecting terms of order H/r or smaller, we find that the equations decouple into two subsystems. One of them corresponds to sound waves propagating in the vertical direction and the other describes MHD perturbations in the plane of the disc, with vanishing z component.

With these simplifying assumptions, the final linear system of equations that describes the MHD perturbations within the disc is,

$$i\omega\rho\boldsymbol{\delta v}_r - 2\rho\Omega\boldsymbol{\delta v}_\phi - \frac{B_0}{c}\boldsymbol{\delta J}_\phi = 0\,, \tag{29}$$

$$i\omega\rho\boldsymbol{\delta v}_\phi + \tfrac{1}{2}\rho\Omega\boldsymbol{\delta v}_r + \frac{B_0}{c}\boldsymbol{\delta J}_r = 0\,, \tag{30}$$

$$i\omega\boldsymbol{\delta B}_r - c\frac{\partial\boldsymbol{\delta E}_\phi}{\partial z} = 0\,, \tag{31}$$

$$i\omega\boldsymbol{\delta B}_\phi + c\frac{\partial\boldsymbol{\delta E}_r}{\partial z} + \tfrac{3}{2}\Omega\boldsymbol{\delta B}_r = 0\,, \tag{32}$$

$$\boldsymbol{\delta J}_r = -\frac{c}{4\pi}\frac{\partial\boldsymbol{\delta B}_\phi}{\partial z}\,, \tag{33}$$

$$\boldsymbol{\delta J}_\phi = \frac{c}{4\pi}\frac{\partial\boldsymbol{\delta B}_r}{\partial z}\,, \tag{34}$$

$$\boldsymbol{\delta J}_r = \sigma_2\boldsymbol{\delta E}'_r - \sigma_1\boldsymbol{\delta E}'_\phi\,, \tag{35}$$

$$\boldsymbol{\delta J}_\phi = \sigma_1\boldsymbol{\delta E}'_r + \sigma_2\boldsymbol{\delta E}'_\phi\,, \tag{36}$$

where $\boldsymbol{\delta E}_\phi$ and $\boldsymbol{\delta E}_r$ are the perturbations of the electric field in the laboratory frame, given by

$$\boldsymbol{\delta E}_\phi = \boldsymbol{\delta E}'_\phi + \frac{B_0}{c}\boldsymbol{\delta v}_r\,, \text{ and} \tag{37}$$

$$\boldsymbol{\delta E}_r = \boldsymbol{\delta E}'_r - \frac{B_0}{c}\boldsymbol{\delta v}_\phi\,. \tag{38}$$

We note that $\sigma_\parallel$, the component of the conductivity tensor parallel to the magnetic field, does not appear in the final linearised equations. Because the ambipolar diffusion and resistive conductivity regimes are differentiated by the value of $\sigma_\parallel$ (section 2.2), this means that during the linear stage of the MRI, under the adopted approximations, these regimes are identical.

3.2 Equations in dimensionless form

Equations (29) to (38) can be expressed in dimensionless form, normalising the variables as follows:

$$z^* = \frac{z}{H} \qquad \rho^* = \frac{\rho(r,z)}{\rho_0(r)} \qquad \boldsymbol{\delta B}^* = \frac{\boldsymbol{\delta B}}{\boldsymbol{B_0}}$$

$$\boldsymbol{\delta v}^* = \frac{\boldsymbol{\delta v}}{c_s} \qquad \boldsymbol{\delta E}^* = \frac{c\boldsymbol{\delta E}}{c_s\boldsymbol{B_0}} \qquad \boldsymbol{\delta E}'^* = \frac{c\boldsymbol{\delta E}'}{c_s\boldsymbol{B_0}}$$

$$\boldsymbol{\delta J}^* = \frac{c\boldsymbol{\delta J}}{c_s\boldsymbol{B_0}\sigma_{\perp_0}} \qquad \boldsymbol{\sigma}^* = \frac{\boldsymbol{\sigma}}{\sigma_{\perp_0}} \qquad \boldsymbol{\sigma}^*_\perp = \frac{\sigma_\perp}{\sigma_{\perp_0}}$$

Subscript 'o' is used to denote variables at the midplane of the disc. Effecting these changes and dropping the asterisks to keep the notation simple, we finally express the dimensionless system of equations in matrix form as:

$$\frac{d}{dz}\begin{pmatrix} B_r \\ B_\phi \\ E_r \\ E_\phi \end{pmatrix} = \begin{pmatrix} 0 & 0 & C_1A_1 & C_1A_2 \\ 0 & 0 & -C_1A_2 & C_1A_3 \\ -\frac{3}{2} & -\nu & 0 & 0 \\ \nu & 0 & 0 & 0 \end{pmatrix}\begin{pmatrix} B_r \\ B_\phi \\ E_r \\ E_\phi \end{pmatrix} \tag{39}$$

$$\boldsymbol{\delta J} = \sigma_\perp C_2\begin{pmatrix} A2 & -A3 \\ A1 & A2 \end{pmatrix}\boldsymbol{\delta E} \tag{40}$$

$$\boldsymbol{\delta v} = \frac{\chi_o}{\rho}\frac{1}{1+\nu^2}\begin{pmatrix} -2 & \nu \\ -\nu & -\frac{1}{2} \end{pmatrix}\boldsymbol{\delta J} \tag{41}$$

$$\boldsymbol{\delta E}' = \frac{1}{{\sigma_\perp}^2}\begin{pmatrix} \sigma_2 & \sigma_1 \\ -\sigma_1 & -\sigma_2 \end{pmatrix}\boldsymbol{\delta J} \tag{42}$$

where

$$\nu = \frac{i\omega}{\Omega}\,, \tag{43}$$

$$C_1 = \chi_o\sigma_\perp\left(\frac{v_A}{c_s}\right)^{-2}C_2\,, \tag{44}$$

$$C_2 = \left[1 + \frac{\chi_o\sigma_\perp}{\rho}\frac{1}{1+\nu^2}\left(\frac{5}{2}\frac{\sigma_1}{\sigma_\perp} + 2\nu\frac{\sigma_2}{\sigma_\perp} + \frac{\chi_o\sigma_\perp}{\rho}\right)\right]^{-1}\,, \tag{45}$$

$$A_1 = \frac{\sigma_1}{\sigma_\perp} + 2\frac{\chi_o\sigma_\perp}{\rho}\frac{1}{1+\nu^2}\,, \tag{46}$$

$$A_2 = \frac{\sigma_2}{\sigma_\perp} + \nu\frac{\chi_o\sigma_\perp}{\rho}\frac{1}{1+\nu^2}\,, \text{ and} \tag{47}$$

$$A_3 = \frac{\sigma_1}{\sigma_\perp} + \frac{1}{2}\frac{\chi_o\sigma_\perp}{\rho}\frac{1}{1+\nu^2}\,. \tag{48}$$

In the above expressions,

$$v_A = \frac{B_o}{\sqrt{4\pi\rho_o}} \tag{49}$$

is the Alfvén speed at the midplane of the disc, and

$$\chi_o = \frac{\omega_{co}}{\Omega} = \frac{1}{\Omega}\frac{B_o^2\sigma_{\perp o}}{\rho_o c^2} \tag{50}$$

is a parameter that characterises the midplane coupling between the magnetic field and the disc (see section 3.3). To understand the information contained in this parameter it is useful to recall that the effect of finite conductivity is different for perturbations of different wavelengths. Finite conductivity is important when the term $c\nabla\times\boldsymbol{E}'$ in the induction equation (3) is of order $\nabla\times(\boldsymbol{v}\times\boldsymbol{B})$. Adoptinga length scale $L \sim 1/k \sim v_A/\omega$ and $\sigma \sim \sigma_\perp$, it is found that these two terms are comparable when $kv_A \sim (c^2/4\pi)k^2/\sigma_\perp$, in other words, non-ideal effects will strongly modify wavemodes at, or above, the critical frequency,

$$\omega_c = \frac{B^2\sigma_\perp}{\rho c^2}\,. \tag{51}$$

It can be shown (W99) that in the limit $|\beta_j| \to \infty$, ω_c reduces to $\sum_j \gamma_j \rho_j$, the collision frequency of the neutrals with any of the charged species. Generally, ω_c is smaller than this value and much smaller than $\gamma_j \rho$, the collision frequency of charged species j with the neutrals. In dense clouds, $\omega_c \sim \gamma_G \rho_G$, which is the smallest $\gamma_j \rho_j$, the collision frequency of neutrals with grains. As $\rho_G \sim 0.01\rho$, the treatment of this paper, restricted to $\omega < \gamma_j \rho$ by neglecting the inertia of the charged species, remains valid for $\omega \sim 100\omega_c$. For perturbations with lower frequencies (longer wavelength) than ω_c, ideal MHD (the flux-freezing approximation) is valid.

3.3 Parameters

As these equations reveal, three important parameters control the evolution of the fluid:

(i) v_A/c_s, the ratio of the Alfvén speed to the isothermal sound speed of the gas at the midplane. It is a measure of the strength of the magnetic field. In ideal MHD unstable modes grow when the magnetic field is subthermal ($v_A/c_s < 1$). When $v_A \sim c_s$ the minimum wavelength of the instability is of the order of the scaleheight of the disc and the growth rate decreases rapidly.

(ii) χ_o, a parameter that characterises the strength of the coupling between the magnetic field and the disc at the midplane (see equation 50). It is given by the ratio of the critical frequency above which flux-freezing conditions break down and the dynamical frequency of the disc at the midplane. If $\chi_o = \omega_{co}/\Omega < 1$ the disc is poorly coupled to the disc at the frequencies of interest for dynamical analysis. As the growth rate of the most unstable modes are of order Ω in ideal MHD conditions, these are also the interesting frequencies for the study of this instability.

(iii) σ_1/σ_2, the ratio of the conductivity terms perpendicular to the magnetic field. It is an indication of the conductivity regime of the fluid, as discussed in section 2.2.

Note that the density of the disc decreases with z, so the local values of χ and v_A/c_s increase with height. The parameters of the model are defined as the corresponding values at the midplane.

It is common practice to characterise the magnetic coupling of a weakly ionised fluid by its electron density n_e. Before finishing this section, we discuss how χ relates to this fluid parameter. We begin by writing the magnetic Reynolds number as (e.g. Balbus & Terquem 2001),

$$\mathrm{Re_M} = \frac{v_A H}{\eta} = \frac{B^2 \sigma_\parallel}{\rho c^2} \frac{\sqrt{4\pi\rho}}{B} \frac{c_s}{\Omega} = \frac{\sigma_\parallel}{\sigma_\perp} \frac{\chi}{v_A/c_s}\,, \tag{52}$$

where we have used $\eta = c^2/4\pi\sigma_\parallel$. If ions and electrons are the only charged species, then

$$\chi = \frac{v_A}{c_s} \frac{\mathrm{Re_M}}{(1+\beta_e^2)^{1/2}(1+\beta_i^2)^{1/2}}\,. \tag{53}$$

In the resistive regime, $|\beta| \ll 1$ for both charged species and (53) shows that the criterion for non-Hall MRI perturbations to grow (W99), $\chi > v_A/c_s$, is equivalent to $\mathrm{Re_M} > 1$.

We can now obtain an expression for χ in terms of the electron fraction $x_e = n_e/n_H$ at the midplane,

$$\begin{aligned} \chi = \frac{1}{\Omega}\frac{B^2\sigma_\perp}{\rho c^2} &= \frac{e n_e B}{c\Omega\rho} \frac{\beta_i - \beta_e}{(1+\beta_e^2)^{1/2}(1+\beta_i^2)^{1/2}} \\ &\approx \frac{n_e < \sigma v > m_e}{(m_e+m_n)\Omega} \frac{\beta_e^2}{(1+\beta_e^2)^{1/2}}\,, \end{aligned} \tag{54}$$

where we used expression (20) for $\sigma_\perp$ and assumed $\beta_i \ll |\beta_e|$. In the above equation

$$< \sigma v > \approx 1 \times 10^{-15} \left(\frac{128kT}{9\pi m_e}\right)^{1/2} \mathrm{cm}^{-2} \tag{55}$$

is the momentum-transfer rate coefficient for electron-neutral scattering. Note that the dependence of χ on magnetic field strength now enters only through the electron Hall parameter β_e. Following Fromang, Terquem & Balbus (2003) we assume that grains have settled out and the electron (and ion) number density is determined by the recombination of metal ions given by,

$$n_e \approx \left(\frac{\zeta n_{\mathrm{H}}}{\alpha}\right)^{1/2}\,, \tag{56}$$

where $\alpha \approx 3 \times 10^{-11} T^{-1/2}\,\mathrm{cm^3\,s^{-1}}$ is the radiative recombination rate for metal ions. The ionisation rate ζ is assumed to be due to cosmic rays at a rate $10^{-17}\exp(-\Sigma/96\,\mathrm{g\,cm^{-2}})\,\mathrm{s^{-1}\,H^{-1}}$ where Σ is the disc surface density. This dominates x-ray ionisation for the column densities we shall consider here. Results are shown in Table 1 for a nominal 1 solar mass star and $B = 10\,\mathrm{mG}$.

For this strength of the magnetic field, $|\beta_e| \ll 1$ at 1 AU and χ scales as B^2 (up to about 200 mG) at this radius. On the other hand, β_e is greater than 1 at 5 and 10 AU, so χ will scale linearly with B (see equation 54). In particular for $B = 100$ mG at 1 AU, $\chi \approx 0.00088$, consistent with the detailed calculations in Wardle (2003).

4 BOUNDARY CONDITIONS

To solve equations (39) to (42) it is necessary first to integrate the system of ordinary differential equations (ODE) in (39). This problem can be treated as a two-point boundary value problem for coupled ODE. Five boundary conditions must be formulated, prescribed either at the midplane or at the surface of the disc.

At the midplane: A set of boundary conditions can be arrived at by asuming fluid variables have either 'odd' or 'even' symmetry about the midplane. 'Odd' symmetry means the variable is an odd function of z and vanishes at $z = 0$. Conversely, when 'even' symmetry is applied, the variable is assumed to be an even function of z and its gradient is zero at the midplane. In this paper we applied the odd - even symmetry criteria to the perturbations in the magnetic field, $\boldsymbol{\delta B}(z) = \pm\boldsymbol{\delta B}(-z)$, where the upper (lower) sign corresponds to even (odd) symmetry conditions. This contrasts with Lovelace, Wang & Sulkanen (1987), who applied the symmetry criteria to the flux function $\Psi(r,z) = rA_\phi$ with A_ϕ the toroidal component of the vector potential and obtained $\boldsymbol{\delta B}_{r,\phi}(r,z) = \mp\boldsymbol{\delta B}_{r,\phi}(r,-z)$ as their symmetry criteria. The symmetry of a particular fluid variable is assigned arbitrarily, subject to the constraint that fluid equations are satisfied. This means that two sets of boundary conditions

Table 1. Comparison of the magnetic coupling parameter χ_o and the ionisation fraction x_e at the midplane for different radial positions r_o, with $B = 10$ mG and assuming grains have settled out (Fromang, Terquem & Balbus 2002). Also shown are the assumed temperature T_o and calculated values of n_H, v_A/c_s, ζ, β_e and β_i.

r_o (AU)	T_o (K)	n_H (cm^{-3})	v_A/c_s	ζ (s^{-1}H^{-1})	$\lvert\beta_e\rvert$	β_i	x_e	χ_o
1	280	6×10^{14}	0.00076	5.76×10^{-22}	0.035	7.68×10^{-5}	7.32×10^{-13}	8.9×10^{-6}
5	130	7×10^{12}	0.010	4.81×10^{-18}	4.44	6.58×10^{-3}	5.11×10^{-10}	1.9
10	90	1×10^{12}	0.033	9.76×10^{-18}	37.31	0.046	1.76×10^{-9}	19

are equally valid, obtained by reversing the assumed symmetry of the fluid variables. Perturbations obtained with a particular set of boundary conditions are displaced a quarter of a wavelength from those found with the other one. The growth rates of these solutions lie at intermediate points of the curve ν vs k obtained from the local analysis (W99), as expected. Evidently, no generality is lost by focusing in one of these two possible sets of solutions. We compare the growth rate versus number of nodes of perturbations obtained with 'odd' and 'even' symmetry in section 5.2 (Comparison with local analysis). For the rest of the analysis presented in this paper we chose to assign odd symmetry to δB_r and δB_ϕ, so they vanish at $z = 0$. This gives us two boundary conditions at the midplane. As the equations are linear, their overall scaling is arbitrary, so a third boundary condition can be obtained by setting one of the fluid variables to any convenient value. To that effect, we assigned a value of 1 to $\delta E'_r$. Summarising, three boundary conditions are applied at the midplane:

$$\boldsymbol{\delta B}_r = \boldsymbol{\delta B}_\phi = 0, \text{ and}$$

$$\boldsymbol{\delta E}'_r = 1\,.$$

At the surface: At sufficiently high z above the midplane, ideal MHD conditions hold. This assumption is appropriate in this case because the local coupling parameter χ is inversely proportional to the density and so it is stronger at higher z regions where the density is smaller. When $\chi > 10$ the growth rate and characteristic wavenumber of unstable modes differ little from the ideal limit (W99), so even though for simplicity we have assumed the conductivity tensor to be spatially constant, we can assume that flux-freezing conditions hold at the surface and the local dispersion relation is $kv_A = \Omega$ (Balbus & Hawley 1991). As the Alfvén speed increases with $\rho^{1/2}$, the wavelengths of magnetic field perturbations increase with z and given the dependency of ρ with z (see equation 28), must tend to infinity as $z \to \infty$. The displacements in the plane of the disc of an infinitely stretched perturbation should effectively vanish, so δB_r and δB_ϕ should be zero at infinity. This gives us the remaining two boundary conditions required to integrate the system of equations (39). Consistently with them, both $\boldsymbol{\delta E'}$ and $\boldsymbol{\delta J}$ vanish as well.

Interestingly, this solution is consistent with $\boldsymbol{\delta E}$ and $\boldsymbol{\delta v}$ being non-zero at infinity. The only requirement is that the gradient of the velocity in the vertical direction $\partial\boldsymbol{\delta v}/\partial z$ be zero when $z \to \infty$, to prevent any horizontal stretching of the magnetic field. It may seem puzzling at first that $\boldsymbol{\delta v}$ is non-vanishing at infinity. This can be understood taking into account that these perturbations travel to infinity in a finite time t_∞ given by,

Table 2. Comparison of maximum growth rate ν_{max} and number of nodes N of the fastest growing modes for all conductivity regimes and two different locations of the boundary. In all cases $v_A/c_s = 0.1$ and $\chi_o = 10$.

Conductivity Regime	$z/H = 5$ ν_{max}	N	$z/H = 7$ ν_{max}	N
Ambipolar Diffusion	0.7303865	5	0.7303869	5
Hall limit ($\sigma_1 B_z > 0$)	0.7498761	5	0.7498761	5
Hall limit ($\sigma_1 B_z < 0$)	0.7461857	5	0.7461854	5
Comparable conductivities	0.7345455	5	0.7345459	5
Opposite conductivities	0.7340035	5	0.7340039	5

$$t_\infty = \int_0^\infty \frac{dz}{v_{Al}} = \frac{H}{v_A}\int_0^\infty exp\left(-\frac{z^2}{4}\right) dz = \sqrt{\pi}\frac{H}{v_A}\,, \qquad (57)$$

where z is the vertical coordinate in units of the scaleheight H and v_{Al} is the local value of the Alfvén speed. Because of this finite travel time to infinity, the fluid can retain a finite velocity when $z \to \infty$. Furthermore, through equations (37) and (38) it is clear that $\boldsymbol{\delta E}$, the perturbations in the electric field as seen from the laboratory frame, are finite at infinity as well.

These boundary conditions are strictly valid at infinity, but will also hold at a boundary located sufficiently high above the midplane. We chose to locate the boundary at $z/H = 5$ after confirming that increasing this height does not significantly affect either the structure or the growth rate of unstable modes. This can be appreciated in Table 2, which compares the maximum growth rate ν_{max} and number of nodes N (proxy for wavenumber) of the perturbations in all conductivity regimes for two different locations of the boundary. Summarising, the boundary conditions adopted at the surface are:

$$\boldsymbol{\delta B}_r = \boldsymbol{\delta B}_\phi = 0\,,$$

at $z/H = 5$.

This system of equations is solved as a two-point boundary value problem for coupled ODE by 'shooting' from the midplane to the surface of the disc and simultaneously adjusting the growth rate ν and $\boldsymbol{\delta E}'_\phi$ until the solution converges.

5 RESULTS

5.1 Test Models

We solved the system of equations (39) for different conductivity regimes, coupling between fluid components and initial magnetic field strengths. As discussed in section 3.1,

Table 3. Relative values of the components of the conductivity tensor perpendicular to the magnetic field σ_1 and σ_2 and fiducial values of the coupling parameters χ_o (good coupling, poor coupling limits) and v_A/c_s adopted to explore the structure of the perturbations for all conductivity regimes.

Conductivity Regime	σ	χ_o	v_A/c_s
Ambipolar Diffusion	$\sigma_1 = 0$	10, 1	0.1
Hall Limit $\sigma_1 B_z > 0$	$\sigma_2 = 0$, $\sigma_1 > 0$	10, 1	0.1
Hall Limit $\sigma_1 B_z < 0$	$\sigma_2 = 0$, $\sigma_1 < 0$	10, 2	0.1
Comparable conductivities	$\sigma_1 = \sigma_2$	10, 1	0.1
Opposite conductivities	$\sigma_1 = -\sigma_2$	10, 1	0.1

under the linear approximation and disc model adopted in the present paper, the ambipolar diffusion and resistive conductivity regimes are identical, so even though throughout this work we have labelled the case when $\sigma_1 = 0$ as the 'ambipolar diffusion' limit, it should be kept in mind that this condition describes the resistive regime as well. Two different Hall limits exist, as the growth rate of the MRI depends on the orientation of the initial magnetic field with respect to the disc angular velocity vector $\mathbf{\Omega}$ (W99). The case when $\boldsymbol{B}_o$ is parallel (antiparallel) to $\mathbf{\Omega}$ is characterised by $\sigma_1 B_z > 0$ ($\sigma_1 B_z < 0$).

We calculated the growth rate and vertical structure of all unstable perturbations for different conductivity regimes with $v_A/c_s = 0.1$. The degree of coupling between the magnetic field and the neutral component of the fluid was characterised by either $\chi_o = 10$ (good coupling) or $\chi_o = 2$ or 1 (poor coupling). The choice of χ_o for the low coupling analysis is dependent on the conductivity regime of the fluid. We took $\chi_o = 1$ for all regimes, except the Hall ($\sigma_1 B_z < 0$) limit, where $\chi_o = 2$ was adopted as our code fails to converge for $\chi < 2$. In this regime, the local analysis shows that when $0.5 < \chi < 2$ all wavenumbers grow (W99). We believe that this complex structure of the perturbations at ever increasing k prevents our code from converging when $\chi_o < 2$.

We also examined the dependency of the structure of the fastest growing modes, their growth rate and the height of maximum amplitude, with the coupling χ_o and the strength of the magnetic field for all conductivity regimes. To study the effect of the magnetic coupling, the value of v_A/c_s was fixed at 0.1. The impact of the strength of the field was explored for good and poor coupling conditions.

Finally, we studied the dependency of the growth rate of the most unstable perturbations with the coupling χ_o for $v_A/c_s = 0.1$ and 0.01 and with the magnetic field strength for $\chi_o = 10$, 2 and 0.1.

The relative values of σ_1 and σ_2 used to characterise each conductivity regime, together with the values of v_A/c_s and χ_o used to explore the structure of the perturbations are summarised in Table 3.

5.2 Comparison with local analysis

The linear growth of the MRI as a function of wavenumber in a local analysis shows that ν vs k generally takes the form of inverted quadratics (W99). The local wavenumber of the perturbations change with z, so we use the number of nodes of δB_r over the entire thickness of the disc, from $z = -5$ to $z = +5$, as a proxy for the wavenumber k to compare our results with those of W99. Results are shown in Fig. 1 for the ambipolar diffusion and Hall ($\sigma_1 B_z > 0$) limits for good and poor coupling. In both regimes the reduction of the wavenumber of the fastest growing perturbation with χ_o is obtained, as expected from the local analysis. Reducing χ_o also diminishes the growth rate of the instability in the ambipolar diffusion limit, but ν remains unchanged for the Hall regime, as expected from the local results.

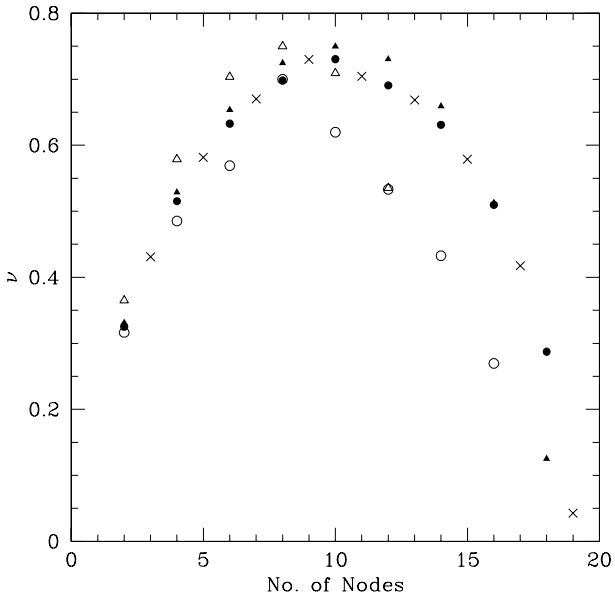

Figure 1. Growth rate versus number of nodes (proxy for wavenumber) of the MRI for different conductivity regimes and coupling at the midplane χ_o. Circles show the ambipolar diffusion limit ($\sigma_1 = 0$) and triangles the Hall limit ($\sigma_2 = 0$, $\sigma_1 B_z > 0$). Filled symbols correspond to the good coupling case $\chi_o = 10$ and open ones to the poor coupling case $\chi_o = 1$. Crosses show the ambipolar diffusion limit with 'even' boundary conditions applied to δB_r and δB_ϕ. Note that results in this case are displaced a quarter of a wavelength (one node) from those obtained with 'odd' boundary conditions. In all cases $v_A/c_s = 0.1$.

These results confirm our expectation that applying boundary conditions and integrating the fluid equations in the vertical direction would restrict the unstable frequencies from the continuous curve ν vs k obtained in the local analysis to a discrete subset of global unstable modes supported by the fluid.

Also shown as crosses in Fig. 1 are the growth rates obtained with 'even' boundary conditions applied to δB_r and δB_ϕ at the midplane (see section 4), for the ambipolar diffusion limit with $\chi_o = 10$. As expected, the perturbations are displaced a quarter of a wavelength (one node) from those obtained with 'odd' boundary conditions.

5.3 Structure of the Perturbations

Fig. 2 shows the perturbations in all fluid variables as a function of height, from the midplane ($z/H = 0$) to the surface of the disc ($z/H = 5$), for the ambipolar diffusion regime and good coupling ($\chi_o = 10$). They are obtained through equations (40) - (42) once the ODE system (39) has been integrated. Note the non-zero values of $\boldsymbol{\delta v}$ and $\boldsymbol{\delta E}$ at the

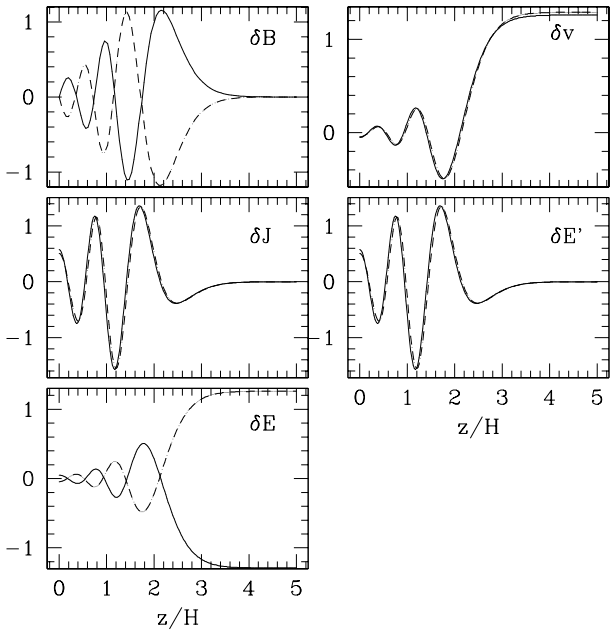

Figure 2. Structure of the perturbations in all fluid variables as a function of height for the most unstable mode in the ambipolar diffusion limit, for good coupling ($\chi_o = 10$) and $v_A/c_s = 0.1$. The growth rate is $\nu = 0.7304$. Note the non-zero values of $\boldsymbol{\delta v}$ and $\boldsymbol{\delta E'}$ at the surface, due to the finite travel time to infinity of the perturbations.

surface, as discussed in section 4. From this point onwards, discussion will be focussed in the perturbations of the magnetic field only. Unless otherwise stated, the radial component of the field δB_r is plotted with a solid line and the azimuthal component δB_ϕ with a dashed line. As the overall scale of our linear equations is arbitrary, plots depicting the structure of the perturbations either do not show the scale of the vertical axis (corresponding to the amplitude of the perturbations) or show a conveniently normalised scale, for reference purposes.

5.3.1 Effect of the Conductivity Regime

Fig. 3 compares the structure of all unstable perturbations for the ambipolar diffusion and Hall ($\sigma_1 B_z > 0$) regimes under good coupling ($\chi_o = 10$). The modes are ordered by the number of nodes. We find that at small ν, the structure of the perturbations in both cases is very similar, but significant differences arise when the growth rate is close to maximum. Then, ambipolar diffusion perturbations peak at the node closest to the surface, while Hall ($\sigma_1 B_z > 0$) ones peak closest to the midplane. This behaviour is linked to the change in the local coupling χ with z and its effect in the structure of the perturbations for different conductivity regimes. It will be discussed further in the next section. At this good coupling level, there are no appreciable differences in the structure or growth rate of perturbations between both Hall limits results, as expected from the local analysis (W99). When both conductivity components are present ($\sigma_1 = \pm\sigma_2$ cases), the structure of the perturbations is similar to the ambipolar diffusion limit. This property is also dependent on the value of the local coupling χ and will be

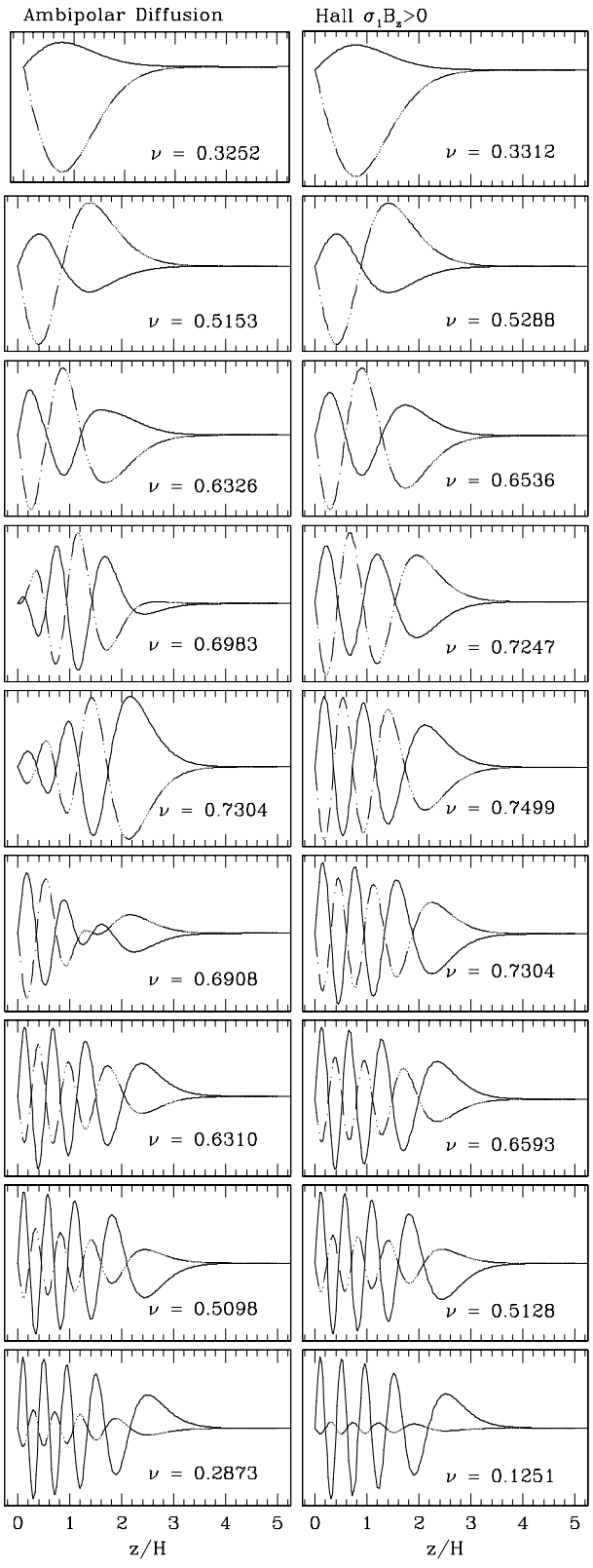

Figure 3. Structure and growth rate of all unstable modes of the MRI for the ambipolar diffusion ($\sigma_1 = 0$) and Hall ($\sigma_2 = 0$, $\sigma_1 B_z > 0$) cases. In all plots $\chi_o = 10$ and $v_A/c_s = 0.1$. For this good coupling, there are no differences between both Hall limits. When both conductivity components are present ($\sigma_1 = \pm\sigma_2$ cases), results resemble the ambipolar diffusion limit shown.

analysed in the next section. We found 9 to 10 unstable perturbations in all cases.

Under low coupling conditions, $\chi_o = 2$ or 1 depending on the conductivity regime (see Table 3), fewer unstable modes grow for both the ambipolar diffusion, Hall ($\sigma_1 B_z > 0$) and the comparable conductivities ($\sigma_1 = \sigma_2$) regimes. Six to eight unstable perturbations are found in these cases. As expected from the local analysis (W99), the range of wavenumbers for which unstable modes exist is reduced as compared with the good coupling cases.

Results are quite different for the two remaining conductivity regimes (Hall $\sigma_1 B_z < 0$ and $\sigma_1 = -\sigma_2$). More unstable modes are found in these cases; 12 in the opposite conductivities case ($\sigma_1 = -\sigma_2$) and a total of 27 for the Hall ($\sigma_1 B_z < 0$) limit. In this last case in particular, despite the low coupling of ionised and neutral components of the fluid, unstable modes have a very complex structure (high wavenumber). Fig. 4 shows the structure of two such modes at the low growth rate, high wavenumber region of the ν - k space. Note that unstable modes are so closely spaced that increasing the number of nodes by a few only maginally changes their wavenumber and has little effect on their growth rate. This complexity is expected from the form of the dispersion relation at low coupling from the local analysis (W99). Non-linear simulations (Sano & Stone 2002a, b) confirm that the many growing modes in this regime strongly interact with each other and the instability develops into MHD turbulence. This turbulence is a transient phase that eventually dies away in two-dimensional simulations (Sano & Stone 2002a) but it is sustained in full three-dimensional models (Sano & Stone 2002b). In both cases the non-emergence of the typical two-channel flow obtained in other regimes is noted by the authors.

Finally, some of the perturbations show a structure resembling an interference pattern (see Fig. 5). They were obtained specifically in regimes where ambipolar diffusion is present, for good and poor coupling, but not in any of the Hall limits. This pattern can be explained recalling that local results show that two unstable modes exist with the same growth rate and different wavenumber. Despite this, just one global mode is found for each ν in this analysis. Again, the application of boundary conditions and integration along the vertical direction restricts global unstable modes from those possible under a local analysis. The interference pattern suggests that global modes are a superposition of two WKB modes with (nearly) the same growth rate and which are not global solutions themselves. The interference of Fig. 5 was successfully replicated through the superposition of two local modes with $\nu = 0.7004$ using the analytical expresions in W99 for the ambipolar diffusion limit.

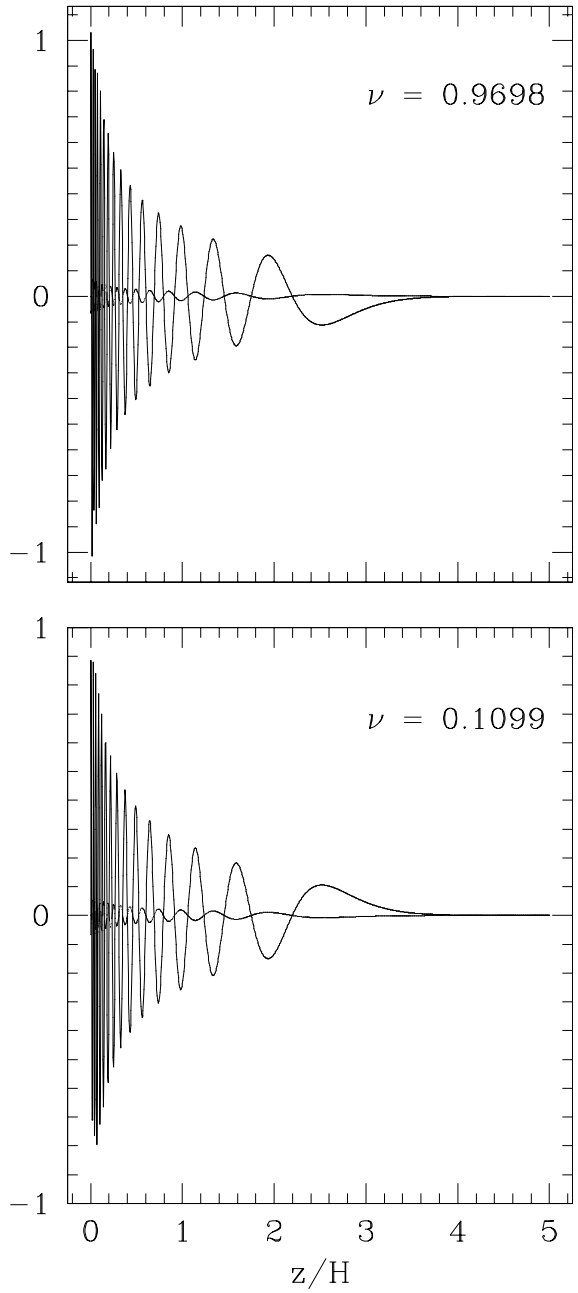

Figure 4. Structure of two unstable modes in the Hall ($\sigma_1 B_z < 0$) limit for poor coupling ($\chi_o = 2$) and $v_A/c_s = 0.1$. Note the complex structure of the perturbations (high wavenumber). Unstable modes are so closely spaced that increasing the number of nodes only marginally changes their wavenumber and growth rate.

5.3.2 Effect of the coupling parameter χ_o

Fig. 6 compares the structure and growth rate of the most unstable modes of the MRI for all conductivity regimes as a function of the coupling parameter χ_o. In all cases $v_A/c_s = 0.1$. We notice that reducing the coupling χ_o causes the wavenumber (i.e. the number of nodes) of unstable modes to diminish in all conductivity regimes except the Hall $\sigma_1 B_z < 0$ limit (rightmost column of Fig. 6), for which this dependency is inverted. The growth rate is also reduced at a rate that depends on the conductivity regime of the fluid. These results are expected from the findings of the local analysis (W99).

It is evident from Fig. 6 that at very high magnetic coupling ($\chi_o \approx 100$), the fluid is close to ideal MHD conditions and results obtained in all conductivity regimes are alike. When the coupling is reduced to $\chi_o \approx 10$, we begin to appreciate differences between them. In particular, the amplitude of the perturbations when ambipolar diffusion is present peaks close to the surface while in both Hall limits the maximum amplitude is closest to the midplane.

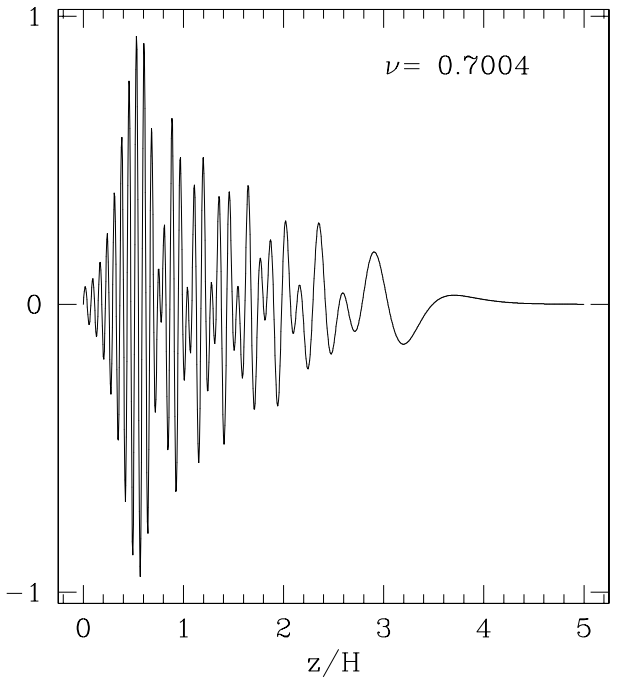

Figure 5. Structure of an unstable mode in the ambipolar diffusion limit ($\sigma_1 = 0$) for good coupling ($\chi_o = 10$) and $v_A/c_s = 0.01$. Note the interference pattern of the perturbation, which suggests that this global mode is a superposition of two WKB modes of similar growth rates.

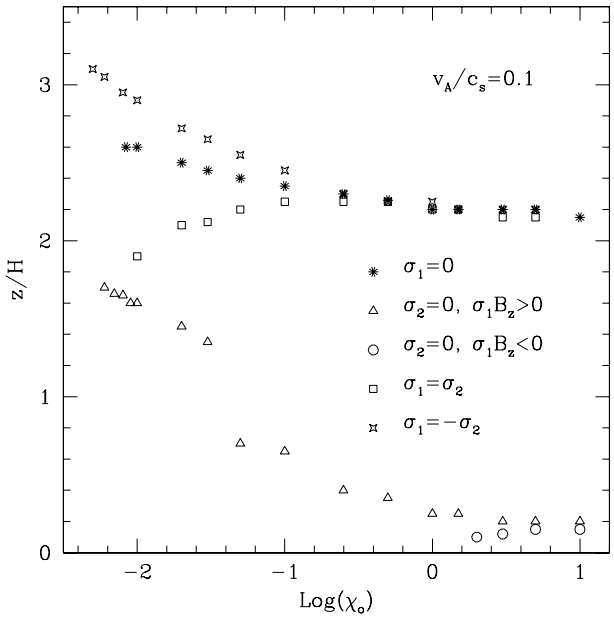

Figure 7. Height of maximum amplitude of the most unstable perturbations as a function of χ_o for all conductivity regimes. In all cases $v_A/c_s = 0.1$

This is more clearly appreciated in Fig. 7, which plots the height of maximum amplitude of the fastest growing modes as a function of the coupling parameter χ_o and the conductivity regime of the fluid for $v_A/c_s = 0.1$. This figure shows that pure Hall regimes ($\sigma_1 B_z > 0$ and $\sigma_1 B_z < 0$) peak closer to the midplane, for all χ_o studied, than the cases when ambipolar diffusion is present. This behaviour can be explained by the dependency of the local growth of the instability with χ for different conductivity regimes. The maximum growth rate of ambipolar diffusion perturbations increases with the local χ (W99), which in turn is a function of height. As a result, at higher z, the local growth of the instability increases, driving the amplitude of global perturbations to increase. Hall ($\sigma_1 B_z > 0$) perturbations, on the contrary, have the same ν_{max} for all χ, so the instability is not driven from any particular vertical location, which explains the flatness of their envelope. This also explains why in Fig. 3 the differences between these regimes are apparent at close to maximum growth: The increment in the local growth rate with the coupling χ is less marked for slow growing perturbations. This is also appreciated in the local analysis by the form of the dispersion relation for different χ in the ambipolar diffusion regime (W99).

It is also clear from Fig. 7 that perturbations in the ambipolar diffusion and Hall ($\sigma_1 B_z > 0$) limits peak at higher z when χ_o is reduced. This dependency is driven by the reduction of the wavenumber of most unstable perturbations with the coupling in these regimes (W99, see also Fig. 6). On the contrary, in the Hall ($\sigma_1 B_z < 0$) limit, the wavenumber of the fastest growing mode increases as χ_o is reduced and the perturbations peak closer to the midplane with weaker χ_o.

Finally, looking at the first three columns of Fig. 6 it is evident that the structure of unstable modes in the $\sigma_1 = \pm\sigma_2$ conductivity regimes are remarkably similar to the ambipolar diffusion limit shown in the leftmost column of the figure for $\chi_o \gtrsim v_A/c_s = 0.1$. When the coupling is weaker than this value, the structure of unstable modes in these regimes is no longer alike. To explain this we recall that the minimum degree of coupling for unstable modes to grow, determined by the requirement that a wavelength fit in the disc scaleheight, is given by $\chi \gtrsim v_A/c_s$ in the ambipolar diffusion limit, and $\chi \gtrsim {v_A}^2/{c_s}^2$ in the Hall case (W99). For $\chi_o \lesssim 0.1$ then, the growth rate of ambipolar diffusion ($\sigma_1 = 0$) perturbations is expected to drop markedly and the envelope of the perturbations will be mainly determined by the Hall effect. This transition in both $\sigma_1 = \pm\sigma_2$ cases, is clearly seen in Fig. 7. In both cases, for $\chi_o \gtrsim 0.1$ the perturbations resemble the ambipolar diffusion limit ($\sigma_1 = 0$). In the $\sigma_1 = \sigma_2$ regime, when $\chi_o < v_A/c_s$ the perturbations resemble those in the Hall ($\sigma_1 B_z > 0$) limit (compare lowest panels in the second and fourth columns of Fig. 6), consistent with the notion that ambipolar diffusion effects are no longer important in this region of parameter space. This implies a constant ν_{max} for weaker χ_o, so the perturbations tend to peak closer to the midplane. On the contrary, in the $\sigma_1 = -\sigma_2$ case, ν_{max} continues to diminish with χ once $\chi < v_A/c_s$ (W99). In this case, the range of growing modes is always finite (as opposed to the Hall $\sigma_1 B_z < 0$ limit) and there is a fastest growing mode for every χ. As a result, the instability is driven at intermediate z (as in the ambipolar diffusion limit) and accordingly, the perturbations peak at higher z with decreasing χ_o. The height of maximum amplitude increases faster as χ_o is reduced in this regime than in the ambipolar diffusion limit. This occurs because ν_{max} for a given local χ is greater in this case (W99, see also section 5.4.1) so global perturbations are amplified even further.

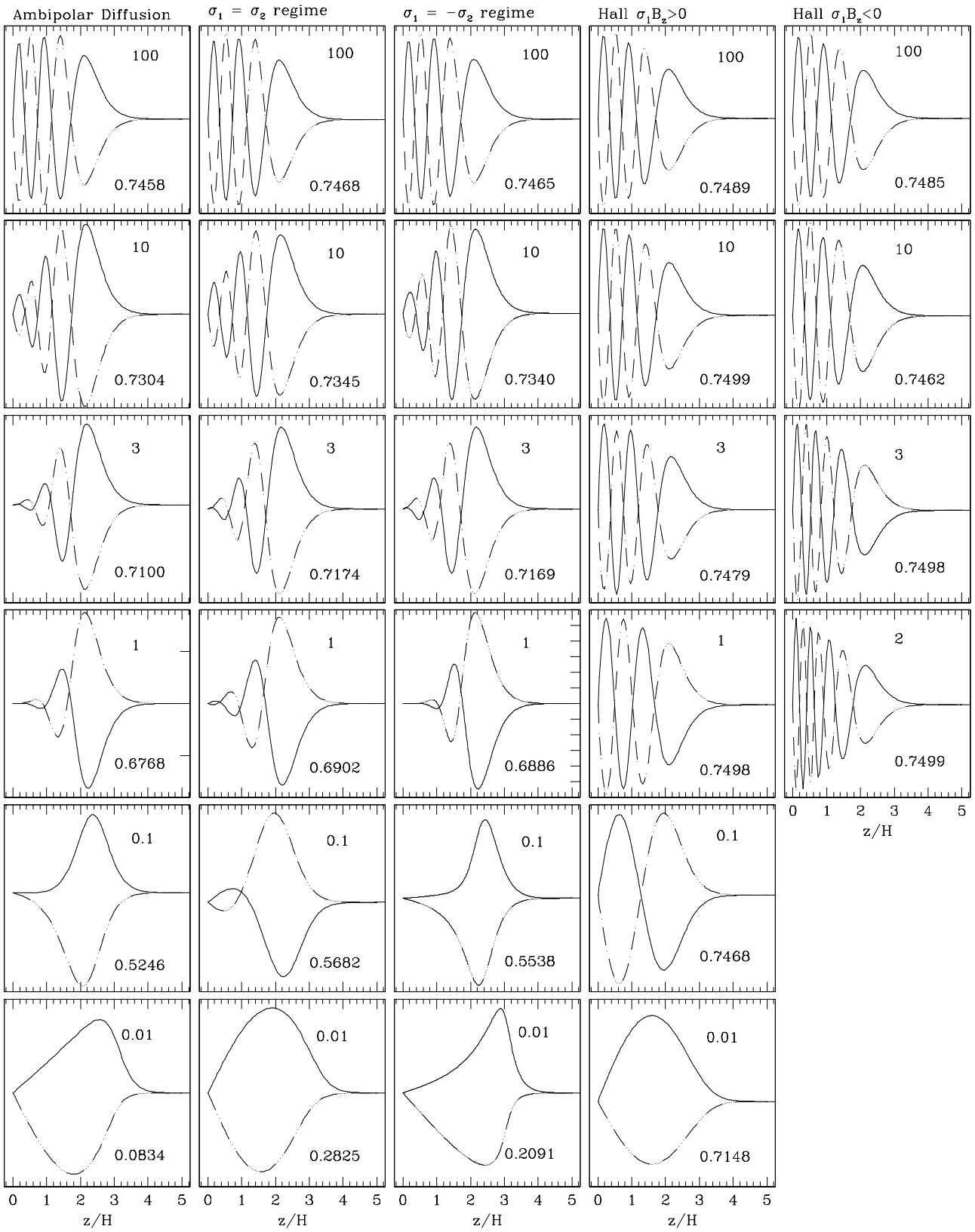

Figure 6. Structure and growth rate of the most unstable modes of the MRI for all conductivity regimes and different values of χ_o. In all cases $v_A/c_s = 0.1$. The value of the coupling parameter χ_o is indicated at the top right corner of each panel. The growth rate (ν) of the perturbations is shown in the lower right corner. Note that the Hall $\sigma_1 B_z < 0$ regime is explored for $\chi_o \geq 2$. In this conductivity regime our code fails to converge for $\chi < 2$ as in this region of parameter space the range of wavenumbers for which local unstable modes exist becomes infinite (W99).

5.3.3 Effect of the Magnetic Field Strength

In ideal MHD, the weaker the magnetic field the higher the minimum wavenumber of the perturbations (Balbus & Hawley 1991). The results of this study are consistent with this finding. With $v_A/c_s \sim 0.005$ the perturbations grow with very high wavenumbers in all conductivity regimes. This can be appreciated in Fig. 8 and 9 for the ambipolar diffusion and Hall ($\sigma_1 B_z > 0$) limits, respectively, for good coupling ($\chi_o = 10$). At this χ_o, solutions for both Hall limits are similar. Also, $\sigma_1 = \pm\sigma_2$ regimes are similar to the ambipolar diffusion limit, as expected. Note the interference pattern of perturbations in lower panels of Fig. 8.

We also studied the dependency of the height of maximum amplitude with the strength of the magnetic field (Fig. 10) for good ($\chi_o = 10$) and poor coupling ($\chi_o = 2$). In the former case, when ambipolar diffusion is present, with and without the Hall effect and regardless of the sign of $\sigma_1 B_z$, the location of maximum amplitude of the fastest growing perturbations as a function of v_A/c_s is similar, which is expected as $\chi_o > v_A/c_s$ (see Fig. 10, panels *a*, *b* and *c*). We obtained unstable modes for v_A/c_s up to 1. As v_A/c_s is reduced from this value, the perturbations peak at higher z until $v_A/c_s \sim 0.04$. However, the location of maximum amplitude begins to diminish as the field is further reduced, which could be caused by the interference pattern, and very high wavenumber, of the perturbations (see also Fig. 8). The height of maximum amplitude peaks at $z \sim 2.8$.

In both Hall limits the height of maximum amplitude increases with the strength of the magnetic field until $v_A/c_s \sim 0.3$ and then remains unaffected with further increments of v_A/c_s (panels *d* and *e* of Fig. 10). This occurs because as the strength of the magnetic field increases, the wavenumber of the perturbations diminish, which pushes the maximum amplitude to higher z. For $v_A/c_s \sim 0.3$ the perturbations have only one node, so any further increase in the magnetic field strength have little effect in the location of the maximum amplitude.

In the low coupling case results are very similar to the $\chi_o = 10$ cases. We note that in regimes where ambipolar diffusion is present (left hand side panels of Fig. 10), perturbations tend to peak at a lower z/H than in the good coupling cases when $v_A/c_s \lesssim 0.1$. In the Hall ($\sigma_1 B_z < 0$) regime, there are unstable modes for 'suprathermal' field strengths (v_A/c_s up to 2.9). This will be further analysed in section 5.4.2, dealing with the dependency of the growth rate of this instability with the strength of the magnetic field. In this case, the height of maximum amplitude peaks at $v_A/c_s \approx 0.5$ and then gradually diminishes as the field is incremented beyond this value.

5.4 The perturbations in parameter space

5.4.1 Effect of the coupling

Fig. 11 shows the growth rate of the most unstable modes as a function of the coupling χ_o for all conductivity regimes with $v_A/c_s = 0.1$ (top panel) and 0.01 (bottom panel). The Hall ($\sigma_1 B_z < 0$) limit could not be modelled for $\chi_o < 2$ because in this region of parameter space the range of wavenumbers for which unstable modes grow becomes infinite (see section 5.1). We find that at the good coupling limit the instability grows at a rate similar to its ideal value

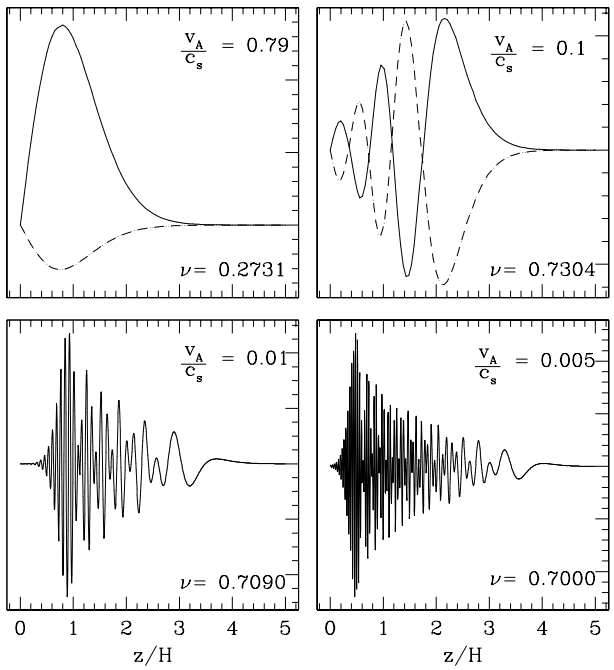

Figure 8. Structure as a function of height and growth rate of the MRI for different choices of v_A/c_s under the ambipolar diffusion limit ($\sigma_1 = 0$) and good coupling $\chi_o = 10$. The value of v_A/c_s is indicated at the top right corner of each panel. The growth rate is shown in the lower right corner.

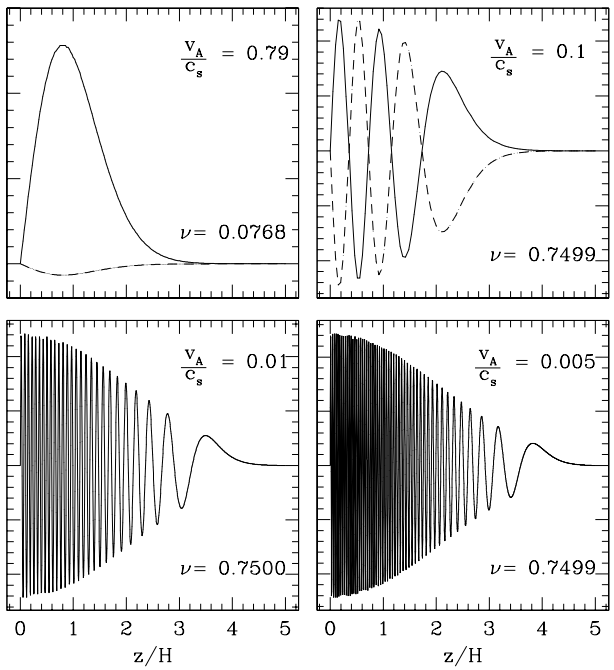

Figure 9. As for Fig. 8, but for the Hall limit $\sigma_1 B_z > 0$. The Hall limit when $\sigma_1 B_z < 0$ (not shown) exhibits the same dependency with v_A/c_s for this χ_o.

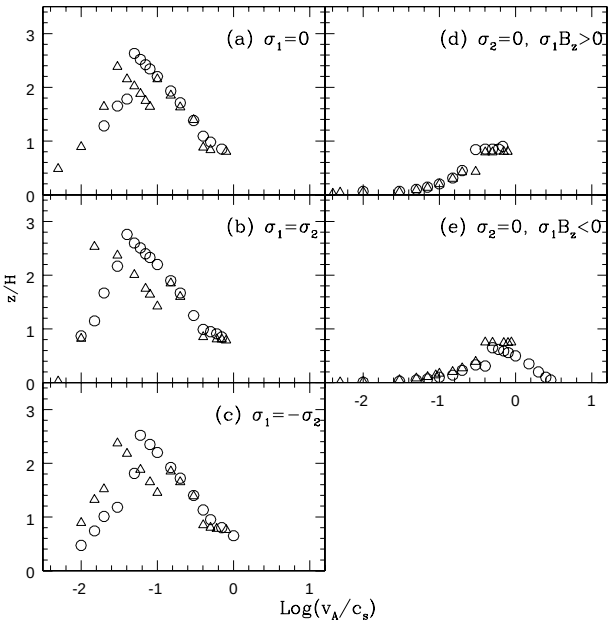

Figure 10. Height of maximum amplitude of the perturbations as a function of v_A/c_s, for all conductivity regimes. Triangles correspond to good coupling ($\chi_o = 10$) and circles to poor coupling ($\chi_o = 2$).

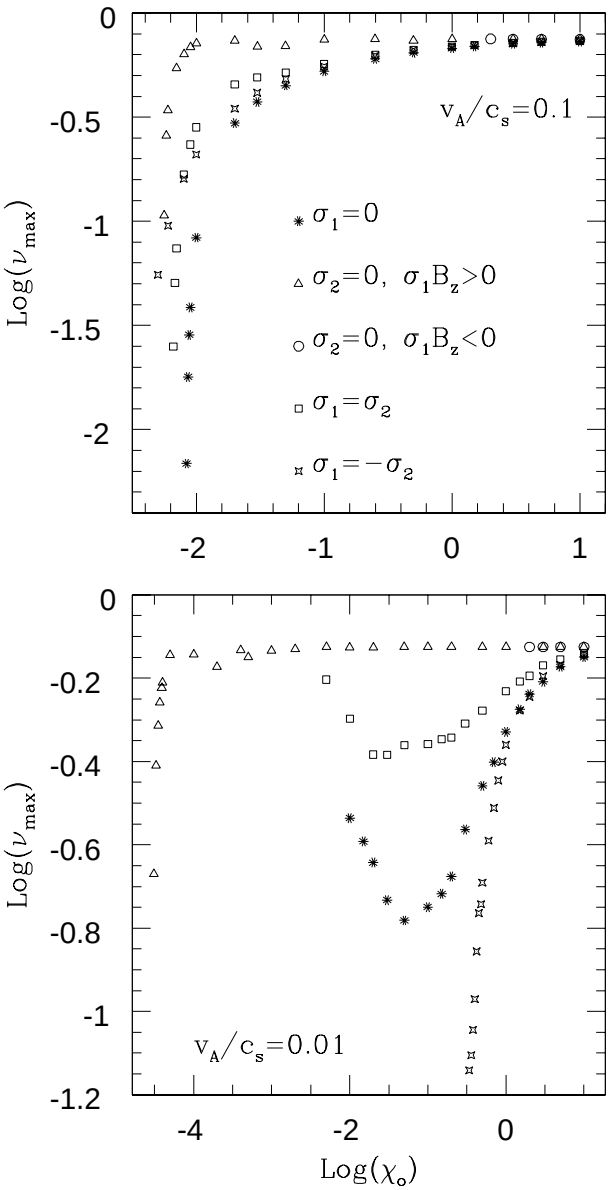

Figure 11. Growth rate of the fastest growing modes of the MRI as a function of χ_o for different conductivity regimes. $v_A/c_s = 0.1$ (top panel) and 0.01 (bottom panel).

of 0.75Ω for all conductivity regimes. As the coupling diminishes, the growth rate is reduced at a rate that depends on the conductivity regime of the fluid. In the Hall ($\sigma_1 B_z > 0$) case the growth rate remains unaffected until $\chi_o \sim 0.01$, and then diminishes drastically to 0.1Ω when $\chi_o \sim 0.005$. The ambipolar diffusion limit has a much more gradual reduction of ν_{max} with χ_o. In this case, the growth rate departs significantly from the ideal value for $\chi_o \sim 0.1$ and then drops rapidly, reaching $\sim 0.007\Omega$ for $\chi_o \sim 0.008$. This is in agreement with findings by W99 that unstable modes grow when $\chi \gtrsim v_A/c_s$ in the ambipolar diffusion limit, and $\chi \gtrsim {v_A}^2/{c_s}^2$ in the Hall case (see also section 5.3.2). When χ is less than these values, perturbations are strongly damped.

When $v_A/c_s \sim 0.01$ (bottom panel of Fig. 11), the growth of Hall ($\sigma_1 B_z > 0$) perturbations is constant at about the ideal rate 0.75Ω until $\chi_o \sim 10^{-4}$. Below this, it plummets to zero as expected. On the contrary, in the ambipolar diffusion and $\sigma_1 = \pm\sigma_2$ regimes, ν_{max} begins to diminish much sooner. It is also noticed that, in the ambipolar diffusion and $\sigma_1 = \sigma_2$ cases, the growth rate increases again after reaching a minimum for $\chi_o \sim 0.05$. This is caused by the high wavenumber of the perturbations due to the weakness of the magnetic field. In these conditions global effects (stratification) are less important and the maximum growth rate diminishes with the coupling as per local results (W99). As the wavenumbers of the perturbations decrease when χ_o is reduced, for sufficiently low χ_o (~ 0.05), k is low enough for global effects to be important again and modify the growth rate of unstable perturbations. With the local χ increasing with height above the midplane, stratification will tend to increase the growth of global modes at low χ_o.

5.4.2 Effect of the magnetic field strength

The dependency of the maximum growth rate with the strength of the magnetic field for all conductivity regimes is shown in Fig. 12 for $\chi_o = 10$, 2 and 0.1. In the good coupling case (top panel), increasing the strength of the magnetic field has little effect in the growth rate of the most unstable modes of all conductivity regimes until $v_A/c_s \sim 1$, where it drastically drops to zero. These results are similar to the ideal MHD case, which predicts that at this strength of the magnetic field the wavelength of most unstable modes become $\sim$ H, the scaleheight of the disc, and the perturbations are strongly damped.

In the $\chi_o = 2$ case shown in the middle panel, we found unstable modes in the Hall limit ($\sigma_1 B_z < 0$) for v_A/c_s up to 2.9. We know from the local analysis (W99) that once the local $\chi \leq 2$, unstable modes exist for every kv_A/Ω in this

conductivity regime. As a result, even for suprathermal fields ($v_A/c_s > 1$), there are still unstable modes with $kH \lesssim 1$ growing within the disc.

Results for $\chi_o = 0.1$ (bottom panel) show clearly how ν_{max} plummets when $v_A/c_s \gtrsim \chi$ (ambipolar diffusion limit) or ${v_A}^2/{c_s}^2 \gtrsim \chi$ (Hall limit), as expected.

Finally, turning our attention to the dependency of the growth rate of the instability with the field strength at low v_A/c_s, we appreciate in all panels of Fig. 12 that ν_{max} initially increases as v_A/c_s is reduced, until it reaches a maximum. Further reductions in v_A/c_s cause the growth rate to diminish monotonically. Comparing these results with the findings of the local analysis (W99), we can show that the growth rates of global unstable modes at weak magnetic field strengths tend to the local values for the relevant coupling χ_o. This can be explained simply by the increase in wavenumber of unstable modes as v_A/c_s is reduced, which causes global effects (driven by stratification) to be less important. As a result, the growth of global modes does not differ significantly from the local values at the same coupling.

6 DISCUSSION

The solutions presented in the previous sections illustrate the growth and structure of the MRI when different components of the conductivity tensor are dominant throughout the entire cross-section of the disc. Density stratification causes the local growth of unstable modes, and the amplitude of global perturbations, to be a function of height. The envelopes of short-wavelength solutions are shaped by this competition between different growth rates acting at different vetical locations. Moreover, when χ is weak at the midplane, long wavelength perturbations are important and vertical stratification is crucial in determining the growth of global MRI solutions. The results presented in this contribution confirm these expectations.

When the Hall and Pedersen components are comparable, the Hall effect alters the structure and growth of unstable perturbations for $\chi_o < v_A/c_s$. In this region of parameter space, ambipolar diffusion perturbations have negligible growth, but unstable modes that include Hall conductivity still grow at $\nu = 0.2 - 0.3$. Hall $\sigma_1 B_z > 0$ perturbations grow faster than $\sigma_1 B_z < 0$ ones. Furthermore, under a weak magnetic field ($v_A/c_s \lesssim 0.01$), the Hall effect significantly increases the growth rate of unstable modes at low coupling. When it dominates, unstable modes grow at close to the ideal rate for $\chi_o \sim 10^{-4}$.

The height above the midplane where the most unstable perturbations peak is dependent on the conductivity regime of the fluid. Consequently, the vertical location of the active zones within the disc, in which the MRI produces angular momentum transport and disc material is being accreted, is dependent on the configuration of the conductivity tensor. Perturbations including ambipolar diffusion peak consistently higher than those in both Hall limits. Also, for $\chi_o < v_A/c_s$, $\sigma_1 = \pm\sigma_2$ modes peak at different heights, signalling that the Hall effect is dependent on the orientation of the magnetic field with respect to the disc angular velocity vector $\mathbf{\Omega}$. In this region of parameter space, when $\sigma_1 B_z < 0$, modes peak at a higher z than when $\sigma_1 B_z > 0$. The Hall effect does not significantly modify the dependency of the height of maximum amplitude of unstable modes with the strength of the magnetic field for good coupling. In this region of parameter space ambipolar diffusion dominates and causes the perturbations to peak at higher z when v_A/c_s is reduced.

When $\sigma_1 B_z < 0$, Hall perturbations can have a very complex structure (high wavenumber), even at low coupling, and many modes are found to grow. In the non-linear stage, the interaction between these modes causes the MRI to develop into MHD turbulence with non-emergence of the typical two-channel flow obtained in other conductivity regimes (Sano & Stone 2002a, 2002b).

When does Hall diffusion determine the behaviour of the instability? Naively one might propose $|\sigma_1| \gtrsim \sigma_2$ as a criterion, but this ignores the level of coupling between the magnetic field and the gas. For example if $\chi \gtrsim 10$, ideal MHD almost holds and there is little dependence of growth rate and structure on the diffusion regime (see Fig. 3). A useful criterion can be derived using the results of the local analysis in W99 and comparing the maximum growth rates with and without Hall diffusion in the weak-coupling limit. In the absence of Hall diffusion (i.e. $\sigma_1 = 0$), the maximum growth rate for $\chi \lesssim 1$ is $3\chi/4$. When Hall diffusion is present and $\chi \lesssim |\sigma_1|/\sigma_\perp$, the maximum growth rate is either $\frac{3}{4}|\sigma_1|/(\sigma_\perp + \sigma_2)$ if $\sigma_1 B_z > 0$ or the instability is suppressed if $\sigma_1 B_z < 0$. In either case, Hall diffusion dominates the behaviour of the instability when

$$\chi \lesssim \chi_{\rm crit} = \frac{|\sigma_1|}{\sigma_\perp}\,. \tag{58}$$

Thus even when $|\sigma_1| \ll \sigma_2$, the structure and growth rate of the magnetorotational instability are dominated by Hall diffusion if $\chi < |\sigma_1|/\sigma_\perp$. This is easily satisfied, for example, for the nominal conditions at the disc midplane 1 AU from the central protostar (see Table 1), where $|\sigma_1|/\sigma_\perp \approx |\beta_e| = 0.035$ (using eqs. 18 and 20 with $|\beta_e| \gg 1$) and $\chi = 9\times10^{-6}$. At 5 AU, $\chi \approx 2$ and $\sigma_1 \gg \sigma_2$, so Hall diffusion dominates here also. Although these results depend on the assumed magnetic field strength, the conditions under which $\chi < \chi_{\rm crit}$ are so broad that we can conclude that Hall diffusion determines the growth rate and structure of the instability over a large range of radii.

Despite this, Hall diffusion has generally been neglected in studies of accretion discs in favour of the ambipolar diffusion or resistive limits. Here we illustrate the severity of this approximation by comparing the structure and growth rate of the unstable perturbations for a model with $\sigma_1 = \sigma_2$ to those for 'simplified' pure ambipolar/resistive diffusion and Hall ($\sigma_1 B_z > 0$) models obtained by setting σ_2 or σ_1 to zero respectively and reducing the coupling parameter χ_o by a factor of $\sqrt{2}$ to reflect its dependence on $({\sigma_1}^2 + {\sigma_2}^2)^{1/2}$ (see eq. 50). The full model has $v_A/c_s = 0.01$ and $\chi_o = 0.01414$, whereas the the corresponding ambipolar diffusion and Hall limits have $\chi_o = v_A/c_s = 0.01$ and the appropriate values of σ_1 and σ_2 as per Table 3.

The comparison is presented in Fig. 13. The structure and growth rate of pure ambipolar diffusion and Hall ($\sigma_1 B_z > 0$) perturbations are as expected for $\chi_o \approx v_A/c_s$, with the ambipolar diffusion decaying towards the midplane and the envelope of the pure-Hall solutions being fairly constant. In both the ambipolar diffusion and the $\sigma_1 = \sigma_2$ cases

we obtain a magnetic 'dead zone' near the midplane where no perturbations grow (Gammie 1996, Wardle 1997). Comparing the top panel of Fig. 13 with the middle and bottom ones it is clear that the Hall effect modifies both the structure and growth of unstable modes. In particular, the extent of the dead zone is reduced and the growth rate is increased. According to these results, both the depth of the active zones within the disc and the rate of angular momentum transport by unstable modes can be significantly modified by the Hall effect.

Although our solutions incorporate the effect of density stratification on the coupling parameter and the Alfven speed, we have assumed that the components of the conductivity tensor do not vary with height. While this simplification permitted us to compare the behaviour of the instability in different regimes, the conductivities in a real disc will reflect the height-dependence of charged particle abundances and their Hall parameters (see §2.1). Different regimes are expected to dominate at different heights (Wardle 2003).

Nonetheless, it is clear from the simplified comparison presented here that Hall diffusion is an essential part of accretion in low-conductivity discs, and that it determines the extent of the magnetically-inactive 'dead zone' (Gammie 1996, Wardle 1997). Further, Hall diffusion will modify any angular momentum transport within the dead zone that occurs via non-axisymmetric density waves driven by the active surface layers (Stone & Fleming 2003) because it will dominate the marginally magnetically-active regions of the disc just above the dead zone. Hall diffusion may therefore affect the ability of dust grains to settle towards the midplane and begin to assemble into planetesimals (e.g. Weidenschilling & Cuzzi 1993).

7 SUMMARY

In this paper we have examined the structure and linear growth of the magnetorotational instability (MRI) in weakly ionised, stratified accretion discs, assuming an initially vertical magnetic field. This work is relevant for the study of low-conductivity accretion systems, such as protostellar and quiescent dwarf novae discs, where non-ideal MHD effects are important (Gammie & Menou 1998; Menou 2000; Stone et al. 2000). The formulation allows for a height-dependent conductivity but in this initial study we assumed the components of the conductivity tensor were constant with height. The analysis was restricted to perturbations with a vertical wavevector ($k = k_z$), which are the most unstable modes when initiated from a vertically aligned magnetic field (Balbus & Hawley 1991; Sano & Miyama 1999). In this case, the field-parallel component of the conductivity tensor plays no role and the ambipolar diffusion and resistive limits are identical. The linearised system of ODE was integrated from the midplane to the surface of the disc under appropriate boundary conditions and global unstable modes were obtained. The parameters that control the evolution of the fluid are: (*i*) The coupling between ionised and neutral components of the fluid evaluated at the midplane (χ_o), which relates the frequency at which non-ideal effects are important with the dynamical (keplerian) frequency of the disc; (*ii*) the magnetic field strength characterised by the ratio v_A/c_s at the midplane; and (*iii*) the ratio of the components of the conductivity tensor perpendicular to the magnetic field σ_1/σ_2.

In order to explore the growth and structure of unstable modes when different conductivity regimes dominate over the entire cross-section of the disc, we examined the following configurations of the conductivity tensor: $\sigma_1 = 0$ (the ambipolar diffusion or resistive limits), $\sigma_2 = 0$ (both Hall limits $\sigma_1 B_z > 0$ and $\sigma_1 B_z < 0$), and the cases where both effects are important ($\sigma_1 = \pm\sigma_2$).

The main results of this study are highlighted below:

(i) Global modes are a discrete subset from the continuous curve of possible ν vs. k combinations obtained with a local analysis (W99). These unstable modes can be expressed as a superposition of two WKB modes with similar growth rate, which explains the interference patterns found in some of the perturbations.

(ii) Ambipolar diffusion perturbations peak consistently higher above the midplane than solutions where Hall conductivity dominates.

(iii) For good coupling ($\chi_o > v_A/c_s$), the structure and growth of the perturbations are mainly determined by ambipolar diffusion. For a weaker coupling, Hall conductivity significantly modifies unstable modes. In this case, $\sigma_1 = \sigma_2$ perturbations resemble the Hall $\sigma_1 B_z > 0$ limit and peak closer to the midplane while $\sigma_1 = -\sigma_2$ modes have their maximum amplitude closer to the surface.

(iv) Hall limit ($\sigma_1 B_z < 0$) perturbations can have a complex structure (high wavenumber) even for poor coupling ($\chi_o = 2$). There are also many unstable modes, which supports findings that in this case the MRI evolves into MHD turbulence with non-emergence of the two-channel flow obtained in other regimes (Sano & Stone 2002a, 2002b).

(v) As the coupling parameter χ_o is reduced, departure from ideal growth $\nu \sim 0.75$ occurs at a rate that depends on the conductivity regime. Hall limit perturbations grow at close to the ideal limit for $\chi_o > {v_A}^2/{c_s}^2$. In the ambipolar diffusion approximation the growth rate decreases when $\chi_o \lesssim v_A/c_s$. These results are in agreement with predictions from W99.

(vi) The weaker the magnetic field the higher the perturbations peak in all regimes where ambipolar diffusion is present. On the contrary, both Hall limits peak closer to the surface with weaker v_A/c_s.

(vii) Unstable modes grow when v_A/c_s is increased until a critical value $v_A/{c_s}_{crit}$ is reached. At the critical v_A/c_s the growth rate abruptly drops to zero. At good coupling $v_A/{c_s}_{crit} \sim 1$ for all conductivity regimes. At the poor coupling limit ($\chi_o = 2$), results are different only for the Hall regime ($\sigma_1 B_z < 0$). In this case we obtain unstable modes for $v_A/c_s \sim 2.9$.

(viii) At very weak magnetic fields ($v_A/c_s \lesssim 0.01$), global effects are less important, due to the high wavenumber of the perturbations. In this region of parameter space the growth rates of MRI perturbations tend to the corresponding local values for the relevant fluid parameters.

(ix) Hall difussion determines the growth of the MRI when $\chi \lesssim |\sigma_1|/\sigma_\perp$. This condition is satisfied over a large range of radii in protostellar discs.

(x) When the Hall regime dominates near the midplane and ambipolar diffusion is dominant closer to the surface, a larger section of the disc is unstable to MRI perturbations

and unstable modes grow faster than those obtained using the ambipolar diffusion approximation

8 ACKNOWLEDGMENTS

We thank the referee for useful comments which improved the clarity of the final paper.

REFERENCES

Adams F. C., Lin D. N. C., 1993, in Protostars and Planets III, ed. E. H. Levy, J. I. Lunine (Tucson: U. Arizona Press), p. 721
Adams F. C., Emerson J. P., Fuller G. A. 1990, ApJ, 357, 606
Balbus S. A., Hawley J. F., 1991, ApJ, 376, 214
Balbus S. A., Hawley J. F., 1992a, ApJ, 392, 662
Balbus S. A., Hawley J. F., 1992b, ApJ, 400, 610
Balbus S. A., Hawley J. F., 1998, Rev. Mod. Phys., 70, 1
Balbus S. A., Terquem C., 2001, ApJ, 552, 235
Beckwith S. V. W., Sargent A. I., Chini R. S., Güsten R., 1990, AJ, 99, 924
Blaes O. M., Balbus S. A., 1994, ApJ, 421, 163
Cabot W., Pollack J., 1992, Geophys. Astrophys. Fluid Dyn., 64, 97
Chandrasekhar S., 1961, Hydrodynamic and Hydromagnetic Stability (New York, Dover)
Cowling, T. G. 1957, Magnetohydrodynamics (New York: Interscience)
Fleming T. P., Stone J. M., Hawley, J. F., 2000, ApJ, 530, 464
Fromang S., Terquem C., Balbus S. A., 2002, MNRAS, 329, 18
Gammie C. F., 1996, ApJ, 457, 355
Gammie C. F., Menou K., 1998, ApJ, 492, L75
Glassgold A. E., Najita J., Igea J., 1997, ApJ, 480, 344
Hawley J. F., Balbus S. A., 1991, ApJ, 376, 223
Hawley J. F., Balbus S. A., 1995, Publ. Astron. Soc. Aust, 12, 159
Hawley J. F., Stone J. M., 1998, ApJ, 501, 758
Hayashi C., 1981, Prog Theor Phys Supp, 70, 35
Hayashi C., Nakasawa K., Nakagawa Y., 1985, in Protostars & Planets II, ed. D.C. Black, M. S. Mathews (Tucson: Univ. Arizona Press), p. 1100
Igea J., Glassgold A. E., 1999, ApJ, 518, 848
Jin L., 1996, ApJ, 457, 798
Lin D. N., Papaloizou J. C., 1980, MNRAS, 191, 37
Lovelace R. V., Wang J. C., Sulkanen M. E., 1987, ApJ, 315, 504
MacLow M. M., Norman M. L., Königl A., Wardle M., 1995, ApJ, 442, 726
Mathis J. S., Rumpl W., Nordsieck K. H., 1977, ApJ, 217, 425
Menou K., 2000, Science, 288, 2022
Moffatt K., 1978, Magnetic Field Generation in Electrically Conducting Fluids (Cambridge: Cambridge University Press).
Nakano, T., Umebayashi, T. 1986, MNRAS, 218, 663
Nishi R., Nakano T., Umebayashi T., 1991, ApJ, 368, 181
Norman, C., Heyvaerts, J. 1985, AA, 147, 247
Ossenkopf V., 1993, AA, 280, 617
Papaloizou J. C. B.,, Terquem C., 1997, MNRAS, 287, 771
Pringle J. E., 1981, Accretion Discs in Astrophysics, ARA&A, 19, 137
Rozyczka M., Spruit H., 1993, ApJ, 417, 677
Ryu D., Goodman J., 1992, ApJ, 338, 438
Sano T., Miyama S., 1999, ApJ, 515, 776
Sano T., Stone J. M., 2002a, ApJ, 570, 314
Sano T., Stone J. M., 2002b, ApJ, 577, 534
Sano T., Stone J. M., 2003, ApJ, 586, 1297
Sano T., Inutsuka S. I., Miyama S. M., 1998, ApJ, 506, L57
Sano T., Miyama S., Umebayashi J., Nakano T., 2000, ApJ, 543, 486
Stone J. M., Balbus S. A., 1996, ApJ, 464, 364
Stone J., Fleming T., 2003, ApJ, 585, 908
Stone J. M., Hawley J. F., Gammie C. F., Balbus S. A., 1996, ApJ, 463, 656
Stone J. M., Gammie C. F. Balbus S. A., Hawley J. F., 2001, in Protostars & Planets IV, ed. V. G. Mannings, A. P. Boss, S. Russell (Tucson: Univ. Arizona Press), p. 589
Umebayashi T., Nakano T., 1990, MNRAS, 243, 103
Velikhov E. P., 1959, JETP, 36, 1398
Vishniac E. T., Diamond P., 1989, ApJ, 347, 447
Wardle M., 1997, in Proc. IAU Colloq. 163, Accretion Phenomena and Related Outflows, ed. D. Wickramasinghe, L. Ferrario, G. Bicknell (San Francisco: ASP), p. 561
Wardle M., 1998, MNRAS, 298, 507
Wardle M., 1999, MNRAS, 307, 849 (W99)
Wardle M., 2003, preprint (astro-ph/0307086)
Wardle M., Ng C., 1999, MNRAS, 303, 239
Weidenschilling S. J., Cuzzi J. N., 1993, in Protostars & Planets III, ed. E. H. Levy, J. I. Lunine (Tucson: Univ. Arizona Press), p. 1031
Weintraub D. A., Sandell G., Duncan W. D., 1989, ApJ, 340, L69

This paper has been typeset from a TEX/ LATEX file prepared by the author.

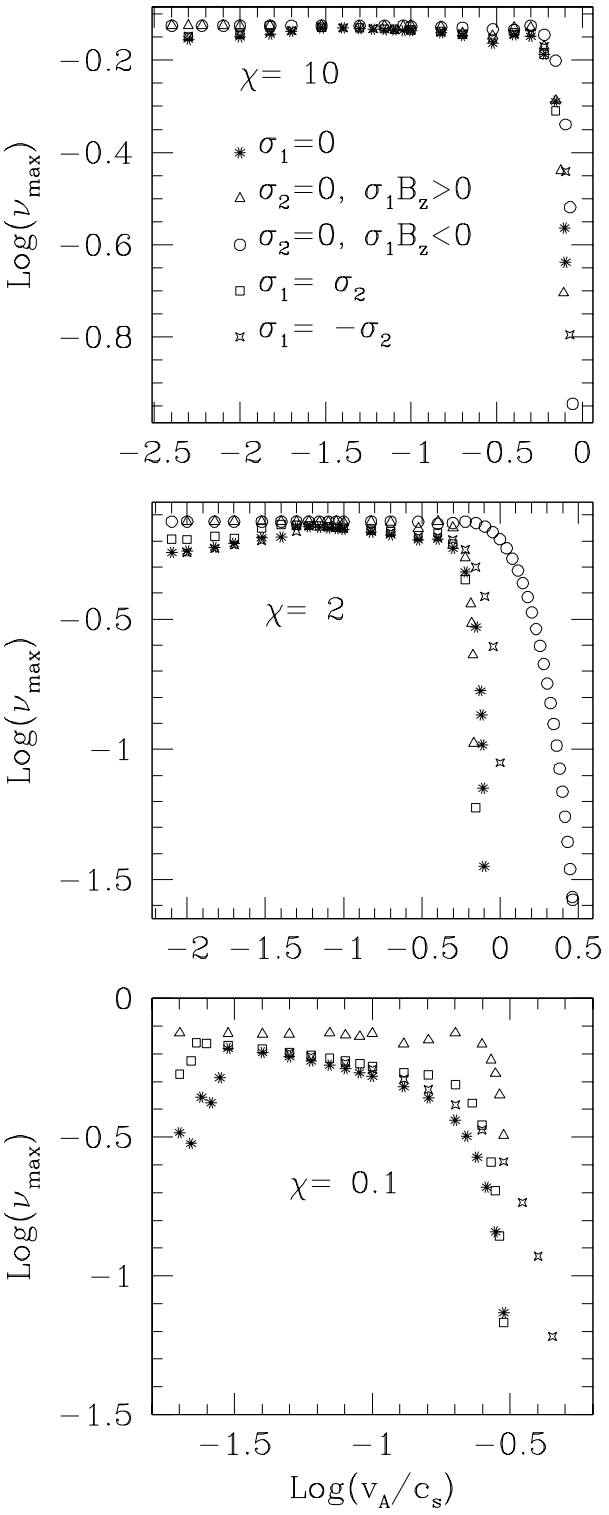

Figure 12. Growth rate of the fastest growing modes of the MRI as a function of v_A/c_s for different conductivity regimes. From top to bottom the coupling χ_o is 10, 2 and 0.1.

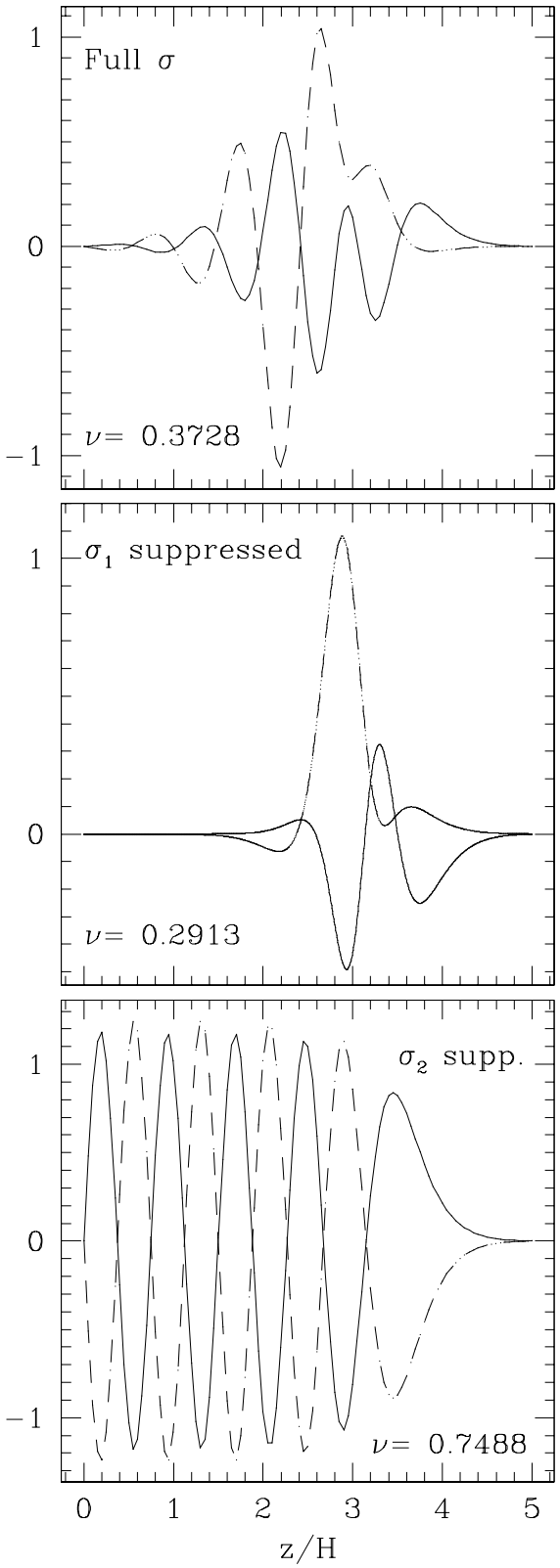

Figure 13. Comparison of the structure and growth rate of the MRI for different configurations of the conductivity tensor for $v_A/c_s = 0.01$. Top panel shows the case where both ambipolar diffusion and Hall ($\sigma_1 B_z > 0$) conductivity terms are important. In this configuration the Hall regime is dominant close to the midplane and ambipolar diffusion dominates near the surface. Middle and bottom panels show the instability under the ambipolar diffusion and Hall approximations, respectively. In the top panel